UNIVERSITÀ DEGLI STUDI DI PARMA

Facoltà di Scienze MM.FF. e NN.

Tesi di Laurea Specialistica in Fisica della Materia

Structural Relaxation and Arrested Dynamics in Gels and Glasses

Relatore:

Luigi Cristofolini

Co-relatori:

Beatrice Ruta

Davide Orsi

Candidato:

Francesco Nazzani

A.A. 2011-2012

"Zhu Ping-man learned how to slaughter the dragons from Zhi-li Yi,
expending all his wealth of a thousand ounces of silver.
In three years he became perfect in the art,
but he never exercised his skill."

-Zhuangzi, 4th century BCE

to my mother,
(who wanted to enrol me in Engineering)

Table of Contents

1 Introduction

This work is about the dynamics of out of equilibrium systems on the microscopic scale, investigated through the X Ray Photon Correlation Spectroscopy (XPCS) technique, and the measurements were done at the ID10 beamline of the European Synchrotron Radiation Facility (E.S.R.F.) in Grenoble.

In the specific case the system studied is a bi-dimensional gel constituted of gold nano particles, confined at the air-water interface, which is a paradigm for a number of interfacial systems of practical relevance in different fields, including food science, cosmetics, medicine, optics, bio-inspired nanotechnology and nanoelectronics industries. As a matter of fact, many advances and improvements have been made possible by a deeper comprehension of the mechanical response and of the internal dynamics of Langmuir films.

This particular film presents a complex and heterogeneous dynamics, in a meta-stable state. Like many other complex systems, such as gels and glasses, its properties depend not only on the external conditions at the time of measurement, but also on its past thermal and mechanical history, and its evolution presents "ageing" phenomena. As a consequence the characterization of the temporal evolution of its dynamics has a fundamental role in the comprehension of his peculiar physical properties.

All these factors contribute to make his study extremely complicated, rising a lot of challenges both from the experimental side, since is difficult to relate results from different experiments and defining measurement protocols that account for each factor, and from the theoretical point of view, because any model needs to account for a lot of parameters.

During the time of my work at E.S.R.F., I also had the opportunity to apply the XPCS technique to other systems, such as structural and metallic glasses. While a detailed discussion of these results is well beyond the scope of the present thesis, some preliminary results will be briefly presented.
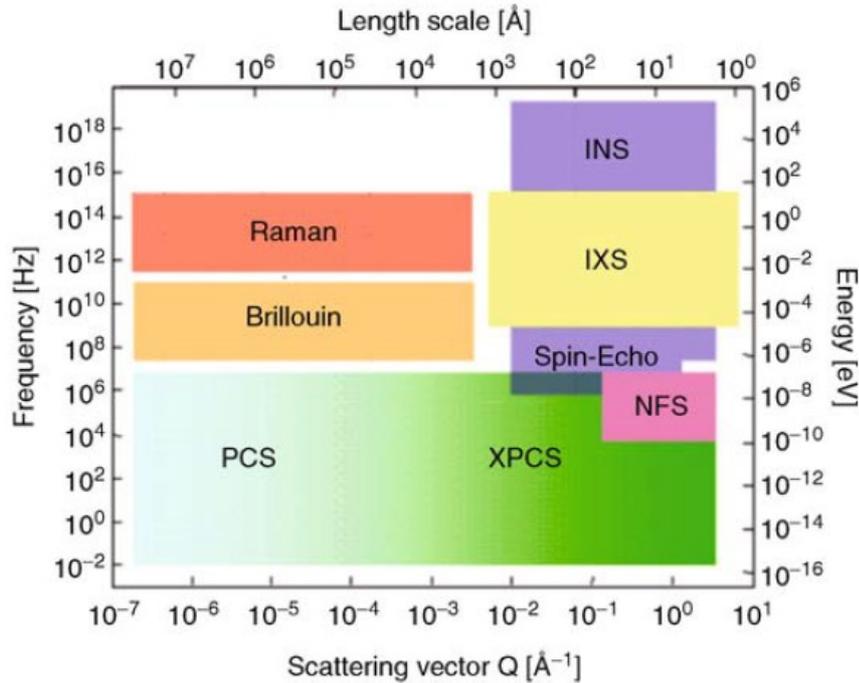
Figure 1.1: Energy - length scale space covered by X-ray Photon Correlation Spectroscopy (XPCS) related to other complementary techniques (Inelastic Neutron Scattering, Raman and Brillouin scattering, Inelastic X-ray Scattering, Neutron Spin-Echo Spectroscopy, Photon Correlation Spectroscopy, Nuclear Forward Scattering)

The XPCS technique has direct access to the length and temporal scales useful for the characterization of out of equilibrium systems, enabling the study of slow and microscopic dynamics, not reached by other techniques. It is an extension in the X-rays domain of the Dynamic Light Scattering employed in the visible regime spectra. It has been developed thanks to the third generation of synchrotron sources, that provide enough coherent flux to compensate for the intensity losses due to the isolation of a coherent beam from the total radiation emitted by the X-ray source.

The system studied is reviewed in the first part of the Thesis, starting from the sample preparation and preliminary characterization obtained from other techniques,

In the third chapter the theoretical background to understand the X Ray Correlation Spectroscopy Technique is discussed , together with the review of some microscopic dynamic models for different kind of system. Then in the last part of the Thesis the XPCS measurements will be reviewed and the experiment results discussed.

2 The Samples

2.1   The gold nanoparticles

The system under investigation is a 2D film of Gold nanoparticles, formed at air-water interface with the Langmuir-Blodgett technique ([1]). The sample is suspended on the surface of water, where the molecules spread and form a layer one molecule thick.

The gold nanoparticles stabilized with a coating of dodecanethiol (Fig. 2.2 and 2.1) were provided by Prof. Ruggeri and his co-workers (University of Pisa), following the procedure described in Refs. [2] and [3].
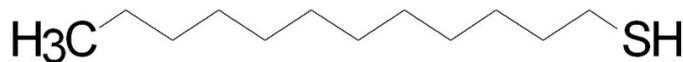
Figure 2.1: Dodecanethiol structure
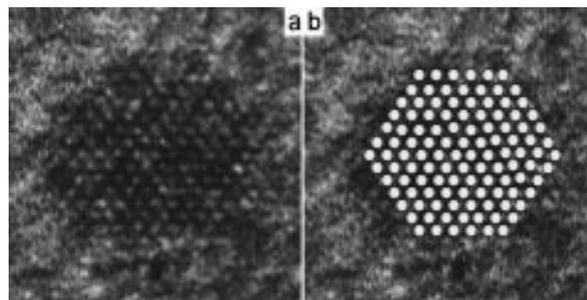
Figure 2.2: Electron microscopy high-resolution micrograph (a) and superimposed schematic atomic diagram (b) of one gold nano-particle viewed from [100] direction. The distances between lattice planes are $d_{111} = 2,35 \ \mathring{A}$ and $d_{200} = 2,03 \ \mathring{A}$. Image taken from Ref. [3].

After the preparation the particles are characterized by a 7nm diameter, but after a month in which the suspension was stored at room temperature (~24°C) they tend to form bigger

aggregates of about 80 nm. This transition is clearly seen by the change in colour of the suspension (Fig. 2.3), that goes from red to violet/blue.
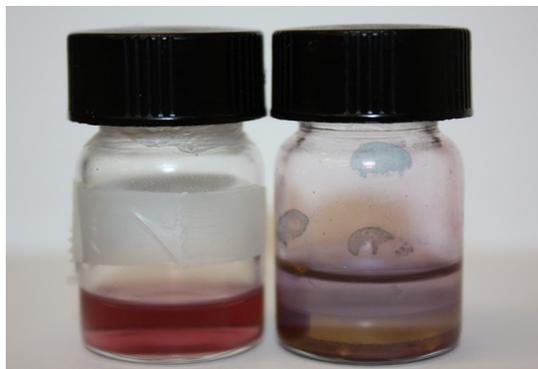
Figure 2.3: on the left, red colloidal suspension of ~7nm nano-particles, on the right the suspension after some time. Note how the violet-blue aggregated particle fill the top part of the solvent.

This change in size has been checked by various techniques as reported in Ref. [4] . Fig. 2.4 shows the UV-Visible absorption spectra as a function of the wavelength, taken on highly diluted hexane solution.
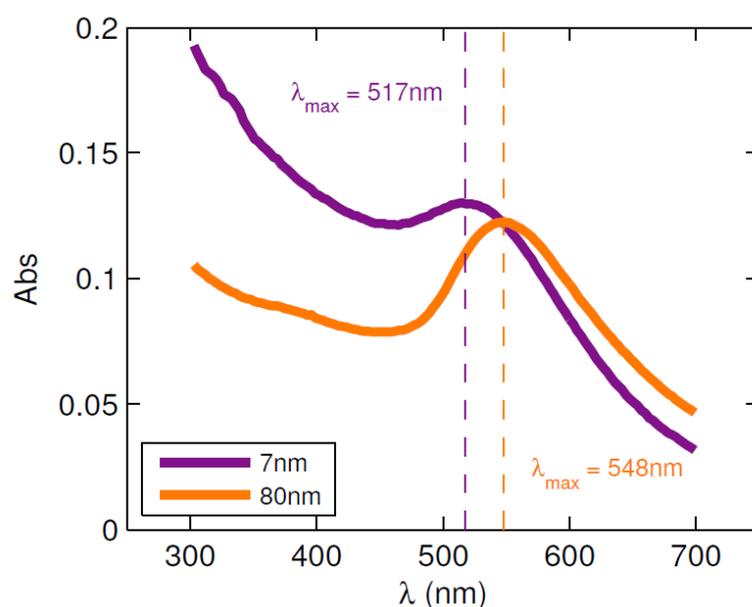
Figure 2.4: UV and visible absorption spectra for 7 nm (blue) and 80 nm (orange) nano-particle suspension, as reported in [4]

The blue line is the one for the "fresh" sample, while the orange is measured after one month: a shift in the absorption peak from 517 to 548 nm, due to the modified surface plas-

mon resonance peak of gold. The estimated diameter was evaluated from these measurements following the procedure described Ref. [5], and confirmed by other measurements obtained through Scanning (SEM) and Transmission Electron Microscopy (TEM).

2.2 The Langmuir film

2.2.1 The Air-water Interface: the Langmuir trough

The systems usually studied at air-water interfaces are mainly composed by surfactants: a large class of molecules significantly important from a technological and biological point of view, the most famous being the common dish soap ([6]).

Surfactants are usually composed by an hydrophilic part (typically polar), commonly referred to as "head", and one hydrophobic (for example one or more saturated alkane chains), called "tails". Such asymmetric molecules naturally prefer the surface of the water, where both their part can minimize interaction energies. Here comes the name "surfactants". Other typical equilibrium configurations that isolates the tails from the water are micelles, where the surfactants form an aggregate suspended in water with the tail insides, or the membranes, where the molecules are disposed in a double layer keeping one of the two phases inside (see Fig. 2.5).
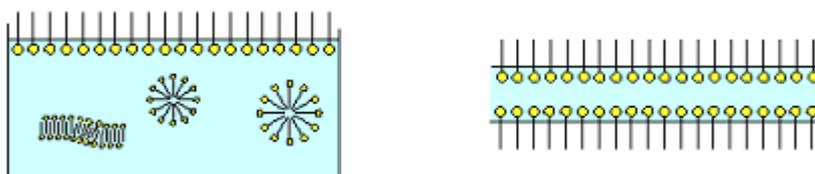
Figure 2.5: Examples of equilibrium surfactants configurations: on the left a monolayers at the interface on the top, and three examples of micelles, on the right a membrane example.

The usual tool for manipulating monolayers is the Langmuir trough: a container of highly polished Teflon, strongly hydrophobic, in which place the water that will constitute the substrate for the deposition. Teflon is employed because it's easily cleanable (water substrate purity is critical) and his hydrophobicity ensures a concave meniscus when the trough is completely filled with water. This effect reduces the formation of collapses and aggregates in the film during his preparation.

The trough has two movable barriers (in teflon as well), so that the available area for the film can be varied, and an internal channels system to control the water temperature (see Fig. 2.6).
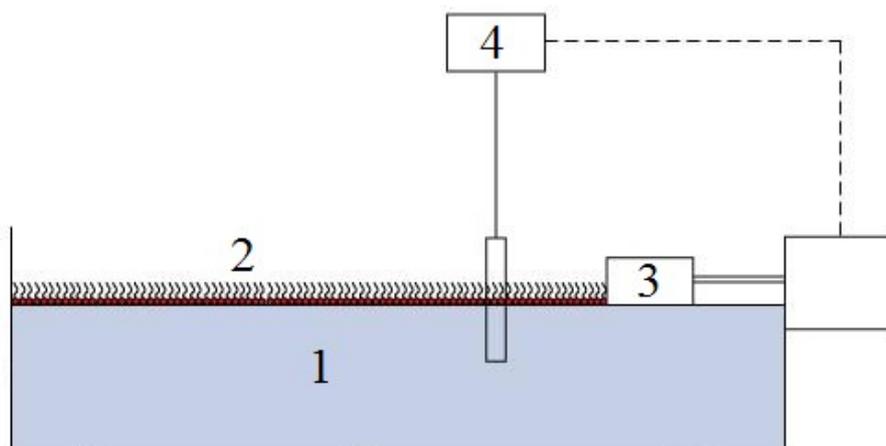
Figure 2.6: A simple scheme depicting a Langmuir trough: on a water subphase (1) surfactants are deposed (2) and compressed by a movable barrier (3). A Whilelmy balance (4) measure the surface pressure and gives feedback to the barrier.

Historically, the classic monolayer experiments were based on surface pressure-isotherm measurements (Fig. 2.7), and the first ones were executed by Agnes Pockels (sister of the more famous Alwink, discoverer the eponymous optical effect) in her kitchen, using a bowl as a water container, two aluminium strips as movable barriers, and a button to measure surface pressure ([7]). She has to be credited for the original design of the trough, later improved by Lord Raylegh first, Langmuir later (who will win the Nobel prize in 1935 for his studies) and then his student Katherine Blodgett. By the way, Agnes Pockel's isotherm of stearic acid is still recognized as essentially correct.

A Langmuir monoalyer is then an excellent model for two-dimensional systems: the water surface provides an ideally smooth substrate, and two thermodynamical variables, temperature and surface pressure, can be directly controlled.

Fig. 2.7, reports an example of an isotherm cycle characterized by a classical behaviour: from right to left we see that reducing the available area, the film this passes through different phases (in analogy to the volume for a gas).
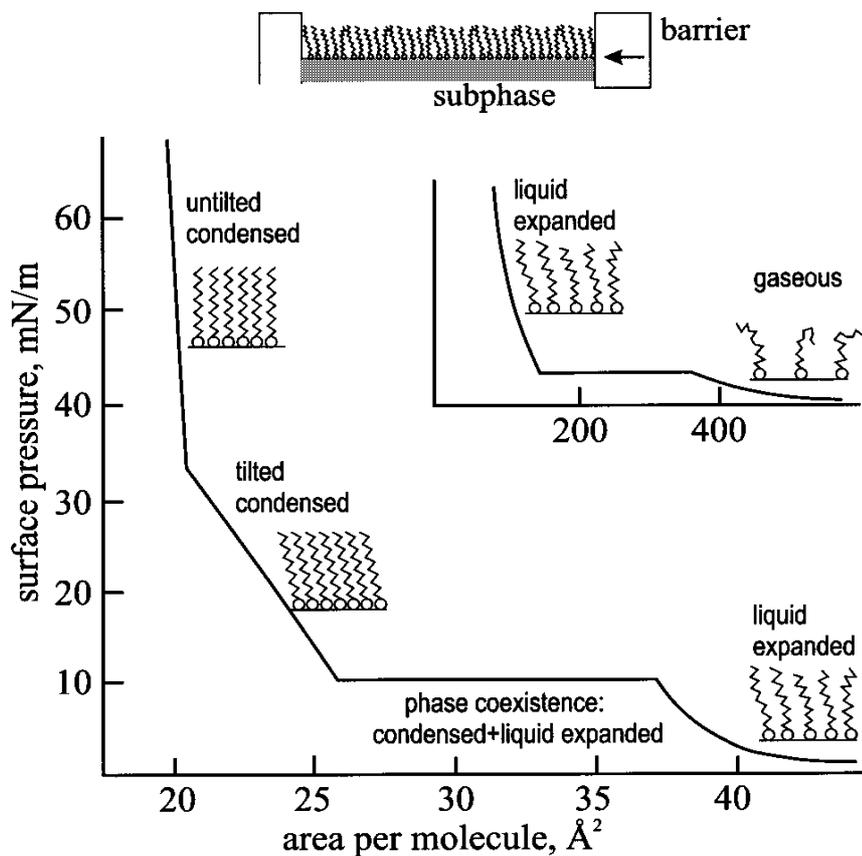
Figure 2.7: Example of Langmuir Isotherms. Reading the graph from right to the left it is seen that as the barrier are pulled together, the area available to the surfactants shrinks, and the molecules assume different phases. This classical case is typical of molecules with no or very weak interaction. From Ref. [1].

Starting in the upper-right inset, when the molecules are far from each other the situation is analogue to a gaseous system. By reducing the available area, after a plateau typical of phase transition, the tails become near enough end the system enters the "liquid" phase. Here the tails start touching each other but the heads are still free to move around, and are not very ordered.

Passing to the main curve in the lower part of Fig. 2.7, after another phase transition plateau, the heads reach a more ordered state, in analogy with a solid phase, and the system becomes more difficult to compress, as seen by the steep increase in the curve that shows how the pressure on the barriers increases very rapidly as the area available to each molecule is reduced.

Upon a further increase of pression, a second "solid" phase is reached, when the tails reorganize themselves and let the heads reach a more efficient packing order.

2.2.2 Surface Pressure: the Whilelmy balance

In equilibrium condition, the attractive forces between the molecules of the liquid result in a net force driving them towards the bulk. This leads them to assume an equilibrium configuration that minimize the exposed surface. This force reacts on every deformation induced on the surface, and it is called *surface tension* (γ). It is defined as the force along a line of unit length, where the force is parallel to the surface but perpendicular to the line, and it has the dimension of a force divided by a length.

The surface tension is measured by a Whilhelmy balance: a thin rectangular plate suspended halfway through the surface. The forces acting on it will be the gravitational pull, the Archimede's push and the effect of the surface tension.

Let's focus the attention on this last contribute: calling θ the contact angle between the water and the sensor, so the surface tension pulls the sensor parallel to the surface tangent on the contact point. The horizontal component of this force is balanced out from the same contribute on the opposite side of the sensor, while the vertical one pulls the sensor down towards the water.
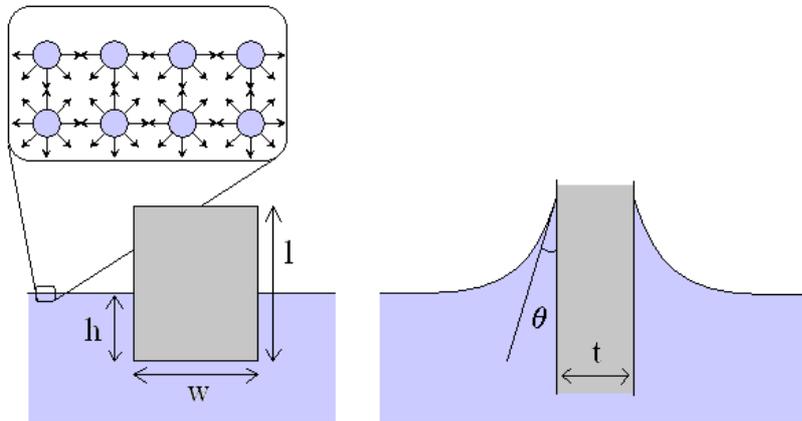
Figure 2.8: in the main panel illustrates a Whilhelmy balance sensor. w, l and t are the total width, length and thickness of the sensor plate, θ the contact angle, and h the submersed height In the upper-left inset, a simple diagram shows water molecules at the surface: in the bulk the total forces result null, instead on the surface a net force towards the bulk of the liquid is present.

Referencing to Fig. 2.8, this net downward force is

$$F = \rho_s lwtg - \rho_{H2O} hwtg + 2\gamma(t+w)\cos\theta \tag{1}$$

where the first two sum terms account for the weight of the sensor and the Archimede's push (ρ_s and ρ_{H2O} are the density of the sensor and the water respectively, and g is the gravity acceleration), while the third term is the one due to the effect of the surface tension.

Studying monolayers, what is investigated is the difference of the surface tension between the free and the monolayer-covered interface. It is then convenient to introduce the *surface pressure* Π, defined as the reduction of the *surface tension* of the liquid due to the film:

$$\Pi \ = \ \gamma_0 - \gamma \tag{2}$$

where γ_0 is the surface tension of the free liquid surface, and γ is the one that characterize the covered one.

Normally the sensor plate is completely wetted in the water, so that $\theta = 1$, and the *surface pressure* Π results from Eq. 1:

$$\Pi \ = \ -\Delta \gamma \ = \ -\frac{\Delta F}{2(t+w)} \ \simeq \ -\frac{\Delta F}{2w} \quad \text{if} \ w \gg t \tag{3}$$

2.2.3 Gel film preparation

The nanoparticles have a more complicated behaviour that the simple surfactants illustrated above. Their dodecanethiol coating is hydrophobic: it stabilizes the particles when they are suspended in an organic solvent, keeping them stable by an hard-sphere-like interaction.

On the contrary, when spread at the air-water interface, the coating reduces the free energy of the configuration and keeps the nanoparticles from subsiding in the water subphase, but provides also a weak, short ranged attractive interaction between them.

This particular structure gives rise to out of equilibrium dynamics, as can be seen in Fig. 2.9: an isotherm series of compression/expansion cycles produces an irreversible compaction of the Langmuir film, as can be seen by the increased steep of the measured Π when decreasing the Area A available to the film.
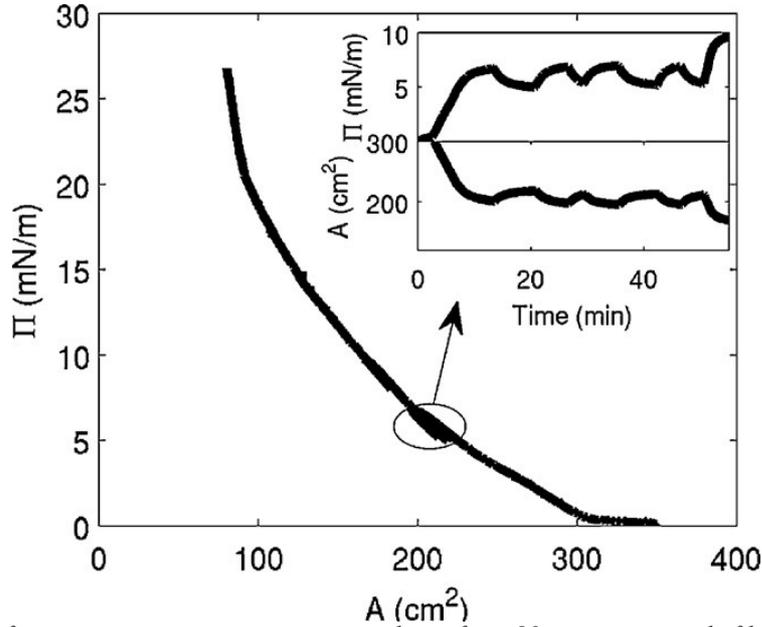
Figure 2.9: Surface pressure–area compression isotherm for a 80 nm nanoparticle film. The surface layer of gold nanoparticles is initially prepared by a careful protocol of spreading and compression–expansion cycles. After the preparatory compression–expansion cycles used to improve the packing of the film, the surface pressure–area compression isotherm shows an upturn and a smooth build-up of pressure. Insets: time evolution of surface pressure Π and of the area A during the compression–expansion conditioning cycles. ([8])

To form the Langmuir monolayer, the original suspension in chloroform was further diluted again with an equal amount of pure hexane, and then picked up and spread on the water surface using a 50 µl Hamilton syringe. The spreading was performed keeping the tip of the syringe in contact with the water surface, with frequent changes of position, until a total of 3 ml were spread. After waiting 15 minutes for the solvent to evaporate, compression started: 5 cycles of slow compressions and expansions between 3 and 5 mN/m were executed to have a better packing in the film. The sample was then brought up to 10 nM/m, at a constant room temperature of 18°C.

Being the sample in an aggregated state, the suspension was no more uniform and was not possible to know the precise concentration of nanoparticles picked up by the syringe, but a good determination of the concentration of spread particles, called packing fraction and defined as

$$\Phi = \frac{Area\ covered\ by\ nano-particles}{Total\ area} \tag{4}$$

can be determined by the surface pressure measurement, as soon as the same compression protocol cycle to form the layer is used.

The right side of Fig. 2.10 shows a sample of the film deposited on a silica substrate, measured with scanning electron microscopy.
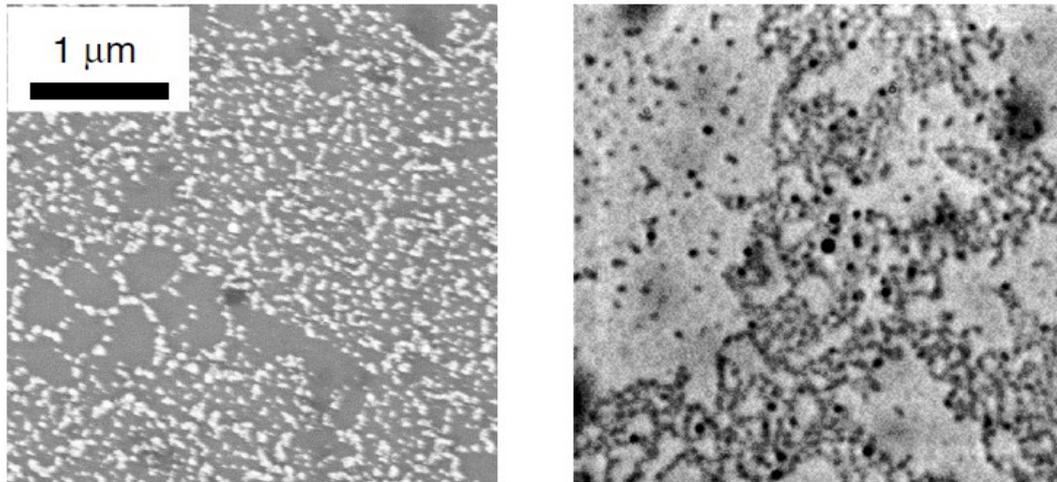
Figure 2.10: Scanning Electron Microscopy images of the gold nanoparticles monolayer deposited on silica. The image on the right comes from Ref. [9], the one on the right is the sample analysed in this work. It is evident that the sample is no more monodisperse, and the distribution of both particles size and free surface between them is broader, and its maximum shifts towards higher values.

The deposited layer shows a very diversified morphology with respect to the "fresh" version of the sample: big aggregated particles are clearly visible as large black dots, and they are distributed between a very inhomogeneous network of smaller ones (in light grey), with some large regions of free surface in between (in light grey). Our sample thus shows a fractal hierarchy of network much more complex than the one observed in the experiment on the "fresh" system reported in Ref.[9], and shown in the right side of Fig. 2.10.

3 X-Ray Photon Correlation Spectroscopy

X-ray Photon correlation spectroscopy (XPCS) investigates the relaxation dynamics of a system from the measurement of the temporal auto-correlation function of the scattered coherent radiation.

Indeed, if coherent light impinges on a sample, it produces a grainy diffraction pattern, called "speckles" pattern, which is related to the exact spatial arrangements of the scatterer units in the material, a mechanism historically used and developed in Dynamic Light Scattering (DLS) experiments ([10]). The same concepts can also be applied to X-ray radiation, so this technique is equivalent to DLS which is a well established method performed with visible light. XPCS uses the partially coherent properties of an X-ray beam ([11]).

Let's consider some monochromatic incident radiation in form of parallel plane waves, interacting with the sample. Each different part of the sample scatters a spherical wave, and all these different contributes interfere at the position of the detector (see Fig. 3.1) which is supposed to be very far from the sample (*far-field approximation*).
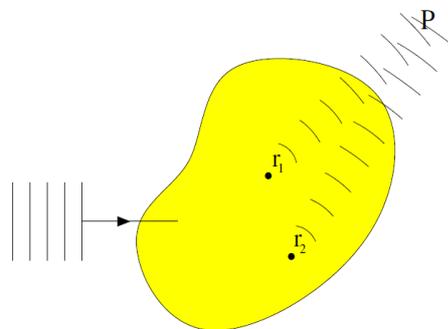

Figure 3.1: Schematic representation of a scattering process: the incident plane wave is scattered from r_1 and r_2, and the scattered spherical waves interferes in P

If one or more of the scatterers move, also the collected interfering waves will evolve with time, originating fluctuations in the scattered intensity and thus in the "speckles" in the diffraction pattern. By monitoring the temporal evolution of the speckles it is therefore possible to get indirect information on the dynamics of the system.

Depending on the wavelength of the incident radiation, it is possible to probe the dynamics at different length scales. For instance visible light corresponds to wavelenghts λ that go from 390 to 750 nm, consequently, using visible light it is possible to investigate the dynamics on the space scale of micron and nanometers.

X-Ray wavelengths instead are much shorter, and correspond to wavevector values between 10^{-3} and several Å^{-1}, so that dynamics down to the atomic scale can be probed. For some samples this has also the additional benefit that only a negligible fraction of the scattered radiation is due to multiple scattering within the sample, which simplifies the interpretation of data. On the downside, the low interaction with matter (the same property that prevents the multiple scattering) reduces also the emitted scattered radiation.

These two factors have limited the development of this kind of studies with X-rays until third generation synchrotrons have been built, providing enough coherent flux ([11]).

3.1   General Theory of Scattering
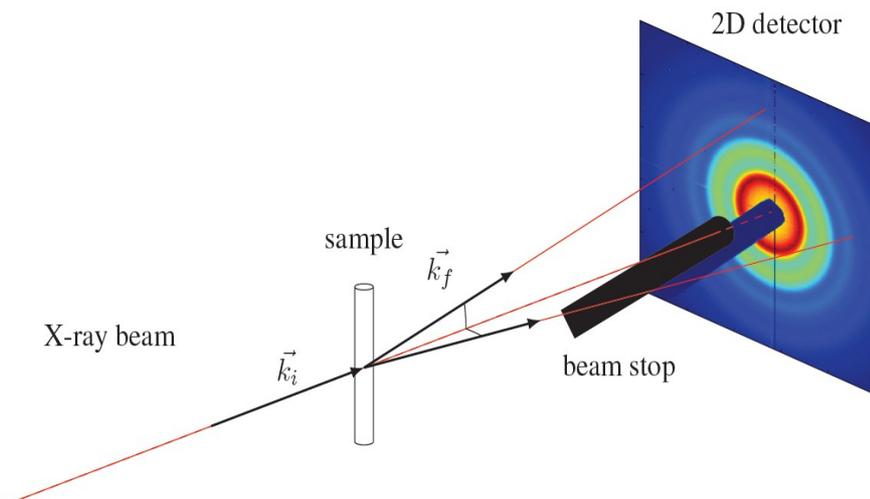
Figure 3.2: A schematic layout of an X-Ray scattering, with incident, transmitted and scattered X-ray beams, sample, and a 2D detector showing an isotropic scattering pattern. $\vec{k}_i$ and $\vec{k}_f$ are the incident and scattered wavevectors, respectively. Note the beam stop that prevent the direct transmitted beam from impinging on the detector.

A schematic layout of a X-Ray scattering process is presented in Figure 3.2: a highly collimated, monochromatic X-ray beam, formed by photons of wavelength λ and wavevector $\vec{k}_i$ of magnitude $|\vec{k}_i| = 2\pi/\lambda$ impinges on a sample and the scattered intensity is recorded by a detector.

Every pixel of the detector collect photons with different wave vectors $\vec{k}_f$, which correspond to a momentum transfer or scattering vector $\vec{q}$ than can be defined as

$$\vec{q} = \vec{k}_i - \vec{k}_f \tag{5}$$
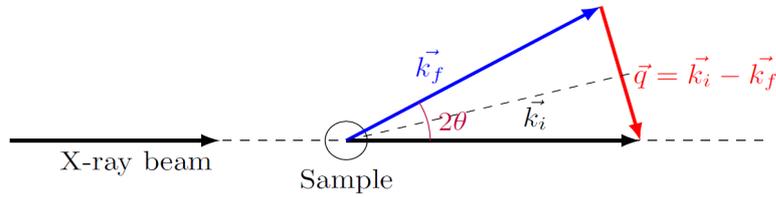
Figure 3.3: Simple scattering geometry: $\vec{k}_i$ is the incident wavenumber $\vec{k}_f$ is the scatttered wavenumber and $\vec{q}$ is the momentum transfer or scattering vector

Since we are considering elastic or quasi-elastic scattering , so that $|\vec{k}_i| = |\vec{k}_f|$, Eq. 5 can be written as (see Fig. 3.3):

$$q = |\vec{q}| = 2k\sin\left(\frac{2\theta}{2}\right) = 2\frac{2\pi}{\lambda}\sin\left(\frac{2\theta}{2}\right) \tag{6}$$

where 2θ is the scattering angle between $\vec{k}_i$ and $\vec{k}_f$, and λ is the wavelength of the incident beam.

3.1.1 Coherent radiation

In the theory so far we have considered a monochromatic plane wave. This is of course an ideal case. As anticipated before the x-ray beam is not perfectly monochromatic, and it is usually divergent, so that photons in different part of the beam have slightly different phases and/or wavevectors, and this difference increases with the distances between them.

For this reasons the resulting signal averages out information on the long distance relations, and carries only the information on short range.

To quantify this characteristic, it is useful to define the concept of *longitudinal* and *transverse spatial coherence*.

Longitudinal spatial coherence takes in account the stability of the wavelength distribution of the beam: the top part of Fig. 3.4 shows two wavefronts with slightly different wavelengths, λ and $\lambda - \Delta\lambda$, that start in phase in point P. Travelling towards the right part of the figure, the two waves build up phase difference due to their different wavelengths, and after a given distance they return in phase. Defining the longitudinal coherence length ξ_L as the distance of maximum phase displacement, it follows that $2\xi_L$ must be the lowest common multiple of λ and $\lambda - \Delta\lambda$:

$$2\xi_L \;=\; N\lambda \;=\; (N+1)(\lambda - \Delta\lambda) \;. \tag{7}$$

Following that $(N+1)\Delta\lambda = \lambda$, for small values of $\Delta\lambda$ $\quad N \simeq \lambda/\Delta\lambda$ and eq. 7 becomes

$$\xi_L \;=\; \frac{1}{2}\frac{\lambda^2}{\Delta\lambda} \;. \tag{8}$$
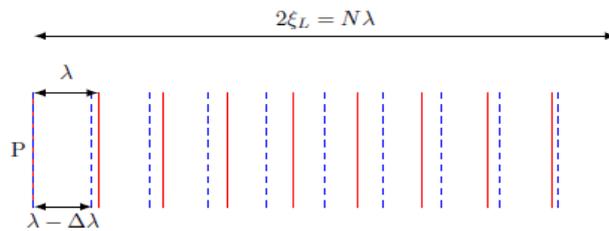
Figure 3.4: Diagram for the definition for the longitudinal coherence: in red and blue two different waves with wavelenghts λ and $\lambda + \Delta\lambda$. The waves are in phase at the starting point P, and return in phase after a distance $2\xi_L = N\lambda$.

Differently, the transverse coherence describes the loss of coherence due to the angular divergence of the beam. Let's start with two waves, A and B, with the same wavelength but that propagate in two different directions, separated by an angle θ, as in Fig. 3.5.

23

The two waves are generated by 2 sources separated by the distance D. They are observed in the plane at the distance R. Starting in P where the two wavefronts coincide and proceeding along the wavefront, we define the transverse coherence length ξ_T by the condition that $2\xi_T$ is the distance after which the two waves are again in phase. Consequently, ξ_T will correspond to the maximum phase shift. For small θ we can write $2\xi_T\theta=\lambda$ and $\theta=D/R$, obtaining:

$$\xi_T = \frac{\lambda}{2}\frac{R}{D} \tag{9}$$
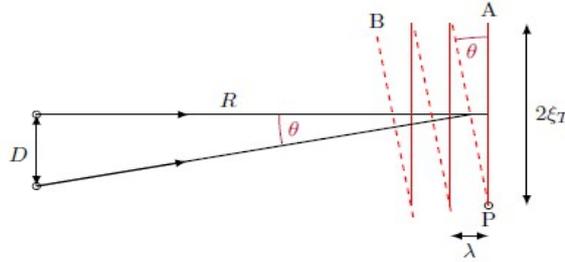
Figure 3.5: Diagram for the definition of the transverse coherence. Two waves (full and dotted lines) propagate along two directions tilted by an angle θ. The two crests of the waves encounter at intervals of
$$2\xi_T = \frac{\lambda}{2}\frac{R}{D}$$

Proceeding from these definitions, a coherent sample illumination is reached when the maximum *Path Length Difference* (PLD) for waves scattered by the sample is smaller or equal to ξ_L and the lateral size of the illuminated sample is comparable to ξ_T, defining the coherence volume as proportional to $\xi_L\xi_T^2$. This quantity is proportional to λ^3, explaining the difficulty of performing coherent X-ray experiments.

More in detail, even with radiation emitted from a synchrotron undulator the beam is never perfectly monochromatic, and typical values of the bandwidth are $\Delta\lambda/\lambda=10^{-2}$, and using a monochromator a resolution of $\Delta\lambda/\lambda=10^{-4}$ can be achieved. Assuming $\lambda\simeq1\,\text{Å}$ this bandwidth give us a longitudinal coherence length of $\xi_L\simeq0.5\,\mu\text{m}$, and for a source-sample distance $R\sim20\,\text{m}$ and a source size $D\sim100\,\mu\text{m}$ results a transverse coherence length of $\xi_T\simeq10\,\mu\text{m}$. This estimate gives us an idea of the length scale

compatible with a coherent illumination, so that the beam spot can be limited to the trans-verse coherence length to have a determined phase relations between all the scattered waves.

3.1.2 Single electron scattering

The usual approach to derive an expression of the scattered intensity begins with the consideration of single electron scattering.

The fundamental quantity measured in a scattering experiment is the *differential scattering cross section* $d\sigma/d\Omega$, which represents the fraction of scattered intensity with respect to the incident one ($d\sigma$) in the solid angle collected by the detector ($d\Omega$). It can be expressed in terms of the Thomson scattering length r_0 as

$$\frac{d\sigma}{d\Omega} = \frac{I_{sc}}{\phi_0 \Delta\Omega} = r_0^2 P \tag{10}$$

where I_{sc} is the intensity scattered, r_0 is

$$r_0 = \frac{e^2}{4\pi\epsilon_0 m c^2} = 2.82\times10^{-5}\,\text{Å} \tag{11}$$

and P is the polarization factor, which depends on the polarization of the incident wave with respect to the selected plane of scattering ([12]). For an incident linearly polarized wave in the horizontal plane P assumes the following values:

$$P = \begin{cases} 1 & \text{vertical scattering plane} \\ \cos^2\theta & \text{horizonthal scattering plane} \end{cases} \tag{12}$$

The classical derivation of equation (10) treats the electron as free to move following the incident plane electric field (for ex. Ref. [13]), and as a source of a spherical wave whose intensity can be evaluated from Maxwell's equations.

It should be noted that the total cross section, as well as the total cross section found by integrating $d\sigma/d\Omega$ over all possible angles, is a constant, independent of the energy

$\frac{hc}{\lambda}$ of the incident radiation. In some cases this assumption is no more valid: for example if the electron is part of an atom, near the absorption edges of an element (the energies corresponding to electron transition or ionization potentials), the interaction of the wave with the electron is more complex.

3.1.3 Single atom scattering

Consider now an atom with Z electrons, whose electron distribution in the volume

V is described by a density $\rho(\vec{r})$ with $\int_V \rho(\vec{r}) = Z$: the scattered radiation field from all the volume V will be the superposition of the contributions from all the different volume elements of this charge distribution, accounting for the phase changes, as in Fig. 3.6.
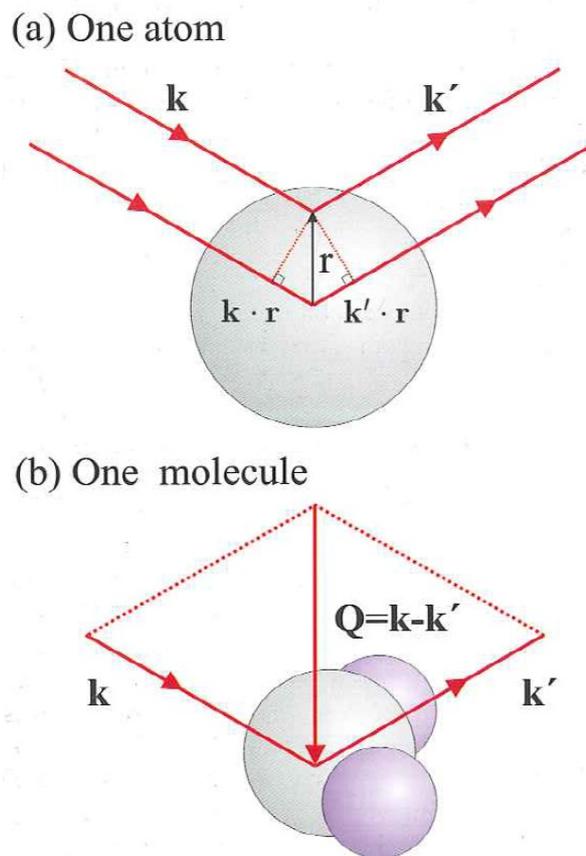
*Figure 3.6: (a) Scattering from an atom. Two incident photons with wavevector $\vec{k}$ scatter in the direction specified by $\vec{k}'$, one from a point in the origin and one in the the position $\vec{r}$. The difference of phase between the two is $(\vec{k}-\vec{k}')\cdot\vec{r}=\vec{q}\cdot r$. (b) Scattering from a molecule. Here is shown the scattering triangle which relates $\vec{k}$, $\vec{k}'$ and $\vec{q}$.*

The total scattering length of the atom will be

$$-r_0 \int \rho(\vec{r}) \exp(i\vec{q} \cdot \vec{r}) d\vec{r} = -r_0 f_0(\vec{q}) \tag{13}$$

where f_0 is called *atomic form factor* and accounts for the different phases of the various spherical waves originated in different places of the sample: taking 2 scatterers separated by the vector $\vec{r}$, the difference in the optical path is $\vec{r} \cdot \vec{k} - \vec{r} \cdot \vec{k}' = -\vec{q} \cdot \vec{r}$. In the limit $\vec{q} \to 0$, f_0 takes the maximum value Z, while for $\vec{q} \to \infty$ the different elements scatter out of phase, and f_0 decreases to zero.

Higher complexity levels (molecules for ex.) can be accounted for, adding the $f_0(\vec{q})$ of different atoms (see Ref. [12]).

3.2   Theory of X-Ray Photon Correlation Spectroscopy

The physical processes presented so far are the basics for all the diffraction techniques, as X-ray diffraction, inelastic X-ray scattering, X-ray tomography, etc. Now we will move on to the specific models for the Dynamic Light Scattering.

3.2.1   Scattering from disordered system

Consider now N different scattering objects suspended in space: the position of the centre of mass of the particle j at the time t is represented by the vector $\vec{r}_j(t)$. Each one of the different N particles will contribute with different phases to the scattered intensity which can be expressed by:

$$I(\vec{q},t) = |\sum_{j=1}^{N} f_j(\vec{q}) \exp(i\vec{q} \cdot \vec{r}_j(t))|^2 \tag{14}$$

To clarify the idea of this situation, consider a prototype situation in which the radiation passes through a a pinhole: in the far field approximation (Fraunhofer), the diffraction pattern can be fully described by the magnitude of the Fourier transform of the function describing the aperture. In the Figure 3.7 (a) is shown a single circle function, and in (b) the

logarithm of the squared magnitude Fourier transform. The concentric rings contain information on the structure of the diffracting object.
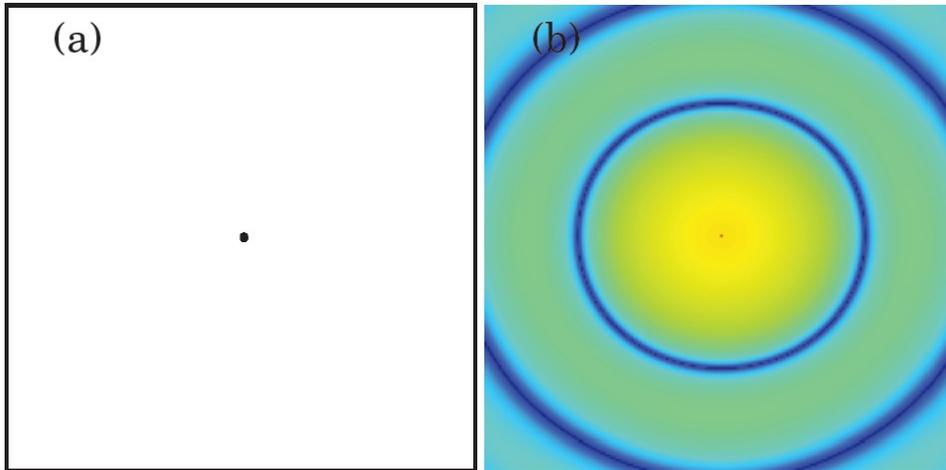
Figure 3.7: (a) a single scatterer point. (b) Logarithm of the magnitude of the Fourier transform of (a).

When a single object is replaced by many, randomly placed ones (Figure 3.8), the individual diffraction patterns interfere with each other, leading to a speckles pattern that encodes the spatial arrangement of the objects, superimposed on the single object ring-like structure.
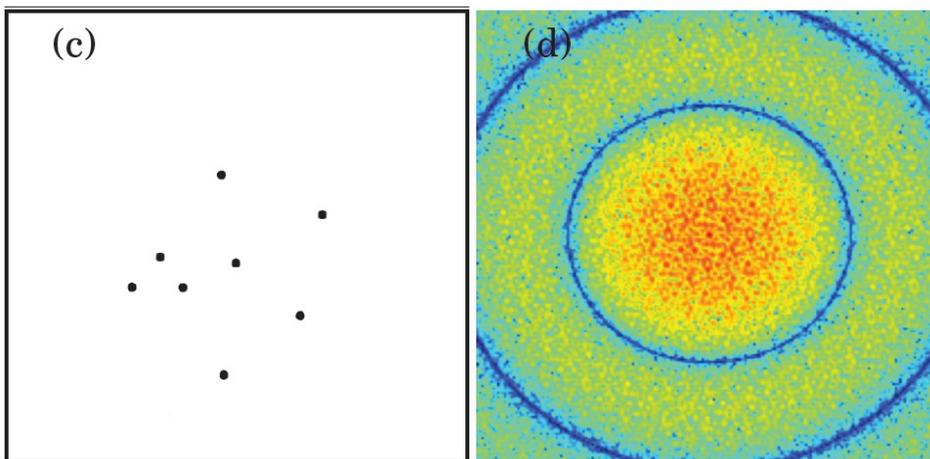
Figure 3.8: (c) Distribution of randomly placed scatterer circles (d) Logarithm of the magnitude of the Fourier transform of the distribution. Above the characteristic ring of the single object diffraction, the speckles pattern is superimposed.

Moving the particles will change the speckles pattern. We can show this by changing the position of a single object, marked with an arrow in Figure 3.9.
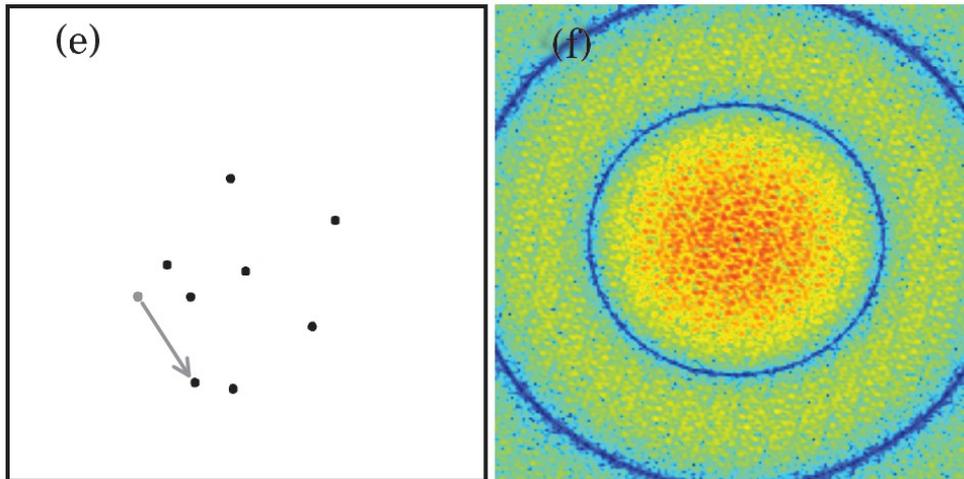
Figure 3.9: displacement of the particle in (e) from his position in 3.8.d. Corresponding logarithm of the magnitude Fourier transform.

To confront the two speckle patterns, Figure 3.10 shows the intensity profile along the diagonal in the two patterns (d) and (f).
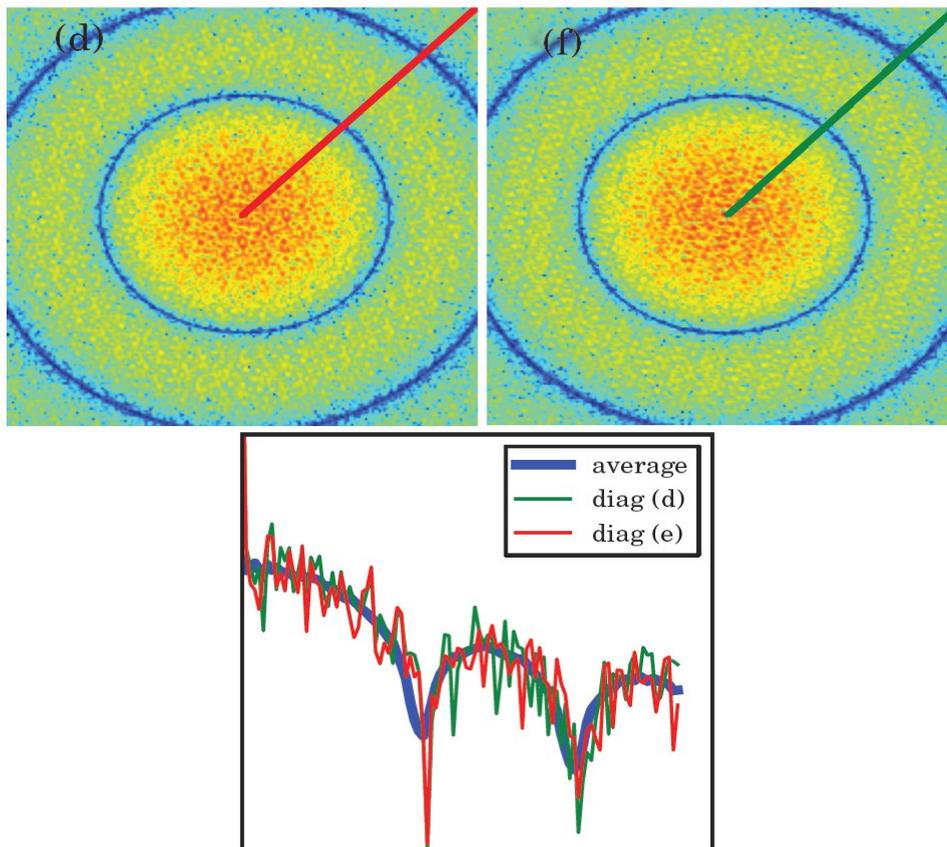
Figure 3.10: A displacement of a single particle between 3.8.c and 3.9.e significantly changes the speckles arrangement in (d) and (f) , as can be seen in the profile reported on the bottom graph.

In an XPCS experiment the detector registers the fluctuating signal of all the moving particles. The signal is then analysed through the determination of the intensity-intensity autocorrelation function. An example is reported Fig. 3.11.
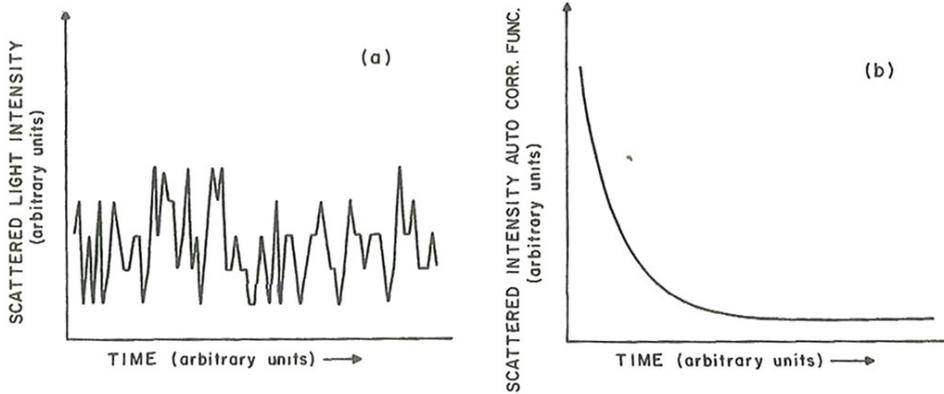
Figure 3.11: a) Intensity of scattered light (arbitrary units) from an aqueous solution of polystyrene spheres of radius 1,01 mm as a function of time (arbitrary units). b) Time-averaged autocorrelation function of the scattered intensity in a) as a function of time in arbitrary units. Taken from Ref. [10]

The signal $A(t)$ can have two very different values in two different times t and $t+\tau$, $A(t){\neq}A(t+\tau)$. If the oscillations are due to the movements of the scatterers instead of random noise, when τ is very small compared to typical times characterizing the aforementioned movements, $A(t+\tau)$ will be very close to $A(t)$, and the deviation of $A(t+\tau)$ from $A(t)$ as τ increases will be more likely to be non-zero. This property can be measured with the autocorrelation function, that confronts the signal $A(t)$ with another version of itself from the future instant $t+\tau$, and can be generally defined as

$$\langle A(0)A(\tau)\rangle = \lim_{t \to \infty} \frac{1}{T} \int_0^T A(t)A(t+\tau)dt \tag{15}$$

where T is the total time of observation, ([10]).

It is important to note that if the scatterers are separated by a distance larger than the coherence lengths, the speckles pattern smooths and the signal resembles the blue average line reported in Fig. 3.10. The same limits apply to the distance covered by the scatterers between two captions between t and $t+\tau$. Thus the maximum Path Length Differ-

ence, as defined in 3.1.1 limits the maximum transferred wavevector q_{max} that can be observed.

3.2.1.1 Intensity autocorrelation function

The quantity investigated in an XPCS experiment is the temporal autocorrelation function of the diffused intensity, so eq. 15 becomes:

$$\langle I_S(\vec{q},\tau)I_S(\vec{q},\tau+t)\rangle_\tau \;=\; \lim_{T\to\infty} \frac{1}{T}\int_0^T I_S(\vec{q},\tau)I_S(\vec{q},\tau+t)\,dt \qquad (16)$$

where the intensity $I_S(\vec{q},\tau)$ measured at the time τ is compared with the intensity $I_S(\vec{q},\tau+t)$ measured at time $\tau+t$.

As shown in Fig. 3.12, for a small delay time t the scatterers seem frozen in place, reducing eq. 16 to

$$\lim_{t\to 0}\langle I_S(\vec{q},\tau)I_S(\vec{q},\tau+t)\rangle_\tau \;=\; \langle I_S^2(\vec{q})\rangle_\tau \;. \qquad (17)$$

Instead for intervals much larger than the typical times of the particles motion, the two positions are completely uncorrelated, and eq. 16 becomes

$$\lim_{t\to\infty}\langle I_S(\vec{q},\tau)I_S(\vec{q},\tau+t)\rangle_\tau \;=\; \langle I_S(\vec{q},\tau)\rangle_\tau\langle I_S(\vec{q},\tau+t)\rangle_\tau \;=\; \langle I_S(\vec{q})\rangle_\tau^2 \;. \qquad (18)$$
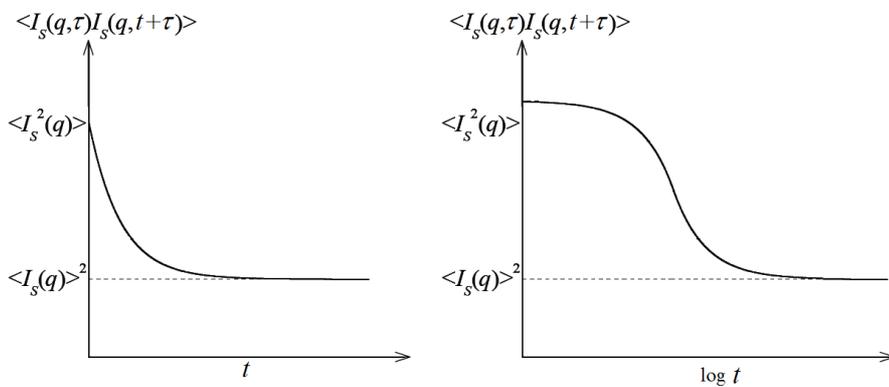

Figure 3.12: on the left: general representation of an intensity autocorrelation function. On the right: same function plotted in logarithmic scale

Considering now all the N particles that contributes to the scattered intensity, we ca insert the expression of I_S from eq. 14 in the expression of eq. 16, obtaining

$$
\begin{aligned}
\langle I_S(\vec{q},\tau) I_S(\vec{q},\tau+t)\rangle_\tau &= f_i \langle \sum_{i=1}^{N}(\vec{q})\exp(i\vec{q}_i\cdot\vec{r}_i(\tau))\sum_{j=1}^{N}(\vec{q})\exp(i\vec{q}_j\cdot\vec{r}_j(\tau+t))\rangle_\tau \\
&= f_i N^2 + f_i N^2 |\langle \exp(-i\vec{q}\cdot(\vec{r}(\tau)-\vec{r}(\tau+t)))\rangle_\tau|
\end{aligned}
\tag{19}
$$

In the second passage we have taken into account the independence of the position of each particle, that means that the only correlation that gives non zero contributions is for a particle with itself ([10]).

This quantity is usually normalized and noted as $g_2(\vec{q},t)$:

$$
\begin{aligned}
g_2(\vec{q},t) &= \frac{\langle I_S(\vec{q},\tau) I_S(\vec{q},\tau+t)\rangle_\tau}{\langle I_S(\vec{q})\rangle_\tau^2} \\
&= 1 + |\langle \exp(-i\vec{q}\cdot(\vec{r}(\tau)-\vec{r}(\tau+t)))\rangle_\tau|^2
\end{aligned}
\tag{20}
$$

It cannot be stressed enough that the angled parenthesis indicate a temporal averaging, and not one performed on every particle of the sample (the statistical *ensemble)*: since the intensity is measured with a time interval Δt, the calculation of $g_2(\vec{q},t)$ is performed starting from a point τ_0, and multiplying $I_S(\vec{q},\tau_0)$ by $I_S(\vec{q},\tau_0+\Delta\tau)$. This value is averaged with every other starting time τ_0 and normalized by $\langle I_S(\vec{q})\rangle^2$ to get the value of $g_2(\vec{q},\Delta\tau)$. Subsequent values of g_2 are then calculated varying the delay time $\Delta\tau$.

This procedures assumes that the value of g_2 is independent from the sample age, so that the system will keep the same behaviour during all the time taken from the measurement: a strong hypothesis, true only if the system is ergodic, so that the temporal mean became equivalent to the ensemble one, or in the case where the temporal evaluation of the dynamics is slower compared to the time interval used to average the g_2 ([14]).

3.2.1.2 The Siegert relation

The experimentally accessible $g_2(\vec{q},t)$ is linked to the function $g_1(\vec{q},t)$ defined as the *Intermediate scattering function* $S(\vec{q},t)$ normalized by the value $S(\vec{q},0)$:

$$g_1(\vec{q},t) = \frac{\langle E_s(\vec{q},0)E_s^*(\vec{q},t)\rangle}{\langle I_s(\vec{q})\rangle} = \frac{S(\vec{q},t)}{S(\vec{q},0)}$$

$$S(\vec{q},t) = \frac{1}{N\langle f_s^2(\vec{q})\rangle}\sum_{n=1}^{N}\sum_{m=1}^{N}\langle f_{s\,n}(\vec{q})f_{s\,m}(\vec{q})\cdot\exp(i\vec{q}(\vec{r}_n(0)-\vec{r}_m(t)))\rangle_{r\in V}$$

(21)

written here for N scatterers, where the angled parenthesis denotes an ensemble average over the scattering volume V (instead of the previous time average), $f_s^2(\vec{q})$ is the square of the scattering amplitude, and $\vec{r}_n(t)$ the position of the n-th scatterer at time t . The intermediate scattering function is thus the normalized Fourier transform of the density-density correlation function f_s , and describes the decay of the density fluctuations an a length scale defined by $2\pi/q$.

If the scattering volume contains a high number of "domains" moving independently one from another, we can treat each scattered electric field as an independent variable. For such a system the central limit theorem is valid and his statistic can be described by a Gaussian distribution. In this particular case it can be demonstrated that the g_2 and g_1 are related by the *Siegert relation* (see Ref. [10] for more details):

$$g_2(\vec{q},t) = 1+\beta|g_1(\vec{q},t)|^2$$

(22)

The parameter β in eq. 22, represents the *contrast*, and is related to the ratio of the coherence volume V_c and the sampled volume V_s . The contrast can vary between 0 and 1 depending on the coherence properties of the beam.

The condition to reduce the ensemble to one with Gaussian distribution is a common one, but it can not be valid any more if the scattering volume is too low: if the scattering volume V can be subdivided into N subregions of volume small compared with the wavelenght of the incident radiation, then the scattered field can be regarded as a superposition of fields from each of the subregions, so that

$$E_S = \sum_{n=1}^{N} E_S(n) \quad . \tag{23}$$

As particles move, $E_S(n)$ fluctuates. If, as is often the case, the subregions are sufficiently large to permit particle motion in one subregion to be independent from those in the others regions, E_S can be regarded as a sum of independent random variables $E_S(1), E_S(2), ...$. In this case Eq. 22 is justified by the central limit theorem so that E_S follows a Gaussian distributions. This situation can be achieved using a 2D detector, so that each pixel registers the signal scattered at the same $\vec{q}$ from an ensemble of different "domains" in the sample, characterized by the same dynamics.

This is a critical condition that can be problematic to obtain in systems characterized by macroscopic domains that moves cooperatively ([15]), from here the necessity to have a coherence volume that contains a significant number of domains. The importance of $g_1(\vec{q}, t)$ function is that it can be predicted by numerical simulations under reasonable conditions.

3.2.2 Models of dynamics

In this section some model of dynamics will be reviewed, to illustrate how the microscopic mobility properties affect the measured correlation function. We will start with the case of Brownian diffusive motion, and from there we will move on to complex models that account for other factors.

3.2.2.1 Diffusive Brownian motion

As an illustration, consider now a simple, monodisperse, suspension of spherical particles undergoing Brownian motion: if the particles are not interacting between them, their positions are statistically independent, and follow a Gaussian probability distribution:

$$P(\Delta \vec{R}\,'(\tau)) = \left(\frac{3}{2\pi 6 \mathrm{D}_0 \tau} \right)^{\frac{3}{2}} \exp\left(\frac{-3 \Delta R^2(\tau)}{2\, 6 \mathrm{D}_0 \tau} \right) \tag{24}$$

In this expression D_0 , the diffusion coefficient for a free particle, is given by the Stokes-Einstein equation:

$$D_0 = \frac{k_B T}{6 \pi \eta a} \qquad \langle \Delta R^2(\tau) \rangle = 6 D_0 \tau \qquad (25)$$

where k_B is the Boltzmann's constant, T the temperature, η the liquid viscosity and a the particle's radius ([16]).

The intermediate scattering function is then written as:

$$
\begin{aligned}
f(\vec{q}, \tau) &= \int \exp(i\vec{q} \cdot \Delta \vec{R}(\tau)) \; P(\Delta \vec{R}(\tau)) \; d^3 \Delta R \\
&= \exp(-\frac{q^2}{6} \langle \Delta \vec{R}(\tau) \rangle) = \exp(-q^2 D_0 \tau)
\end{aligned}
\qquad (26)
$$

Referencing to eq. 22 we can now write the $g_2(\vec{q}, \tau)$ as

$$g_2(\vec{q}, t) = 1 + \beta \exp(-2 D_0 q^2 t) \qquad (27)$$
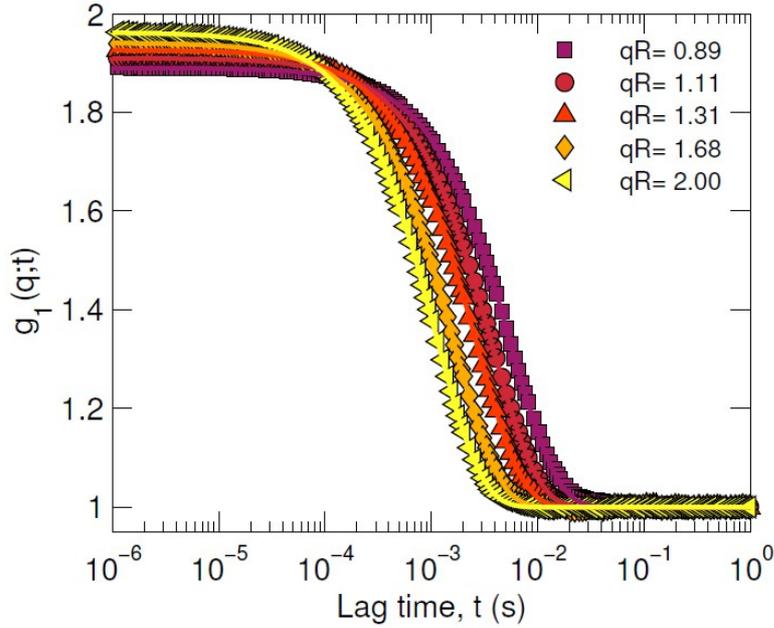
Figure 3.13: $g_1(\vec{q}, t)$ *function measured by DLS on a low concentration suspension of PMMA particles (R=90nm) as reported in ref. [17] . Continuous lines are the best fit lines obtained with eq. 27.*

The factor $D_0 q^2$ is usually written as $1/\tau_c$, marking with τ_c (also called relaxation time) the necessary time for the system to rearrange its structure on a length scale defined by q. In the case of pure diffusion, as in the brownian motion, τ_c scales as $\propto 1/q^2$, and thus it strongly increases for small wavevectors, or large length scales.

3.2.2.2 Dynamics of complex disordered systems: stretched exponential functions

The previous simple expression of eq. 27 does not hold when the interactions between particles are not negligible any more.

Many disordered materials, like molecular glasses, polymers, gels and other soft materials undergo structural arrest (an abrupt slowing down of the dynamics not associated to structural changes) and physical ageing (a change in the dynamics parameters in macroscopic time scale). In fact, by modifying different characteristics of the system (like the temperature, the packing fraction, or the polymer concentration) these materials can be driven in an out of equilibrium configuration, where the dynamics slows down enormously, and strongly depends on the sample age or waiting time (see for examples Ref. [18] and Ref. [19]).

The slowing down of the dynamics leads to a complex shape of the intermediate scattering function which can not be any more described by a single exponential decay, as is the case in Brownian motion.

This effect has been accounted for by two complementary approaches: *Mode Coupling Theory* (MCP, [20]) and *Potential Energy Landscape* (PEL, [21]).

MCT describes the local dynamics of molecules in the supercooled liquid phase close to the glass transition temperature (T_G): every particle results confined in a "cage" by collision with its neighbours, so that after an initial decay due to microscopic collisions inside this cage, the correlation function shows a plateau followed by a secondary decay on longer time scales, that is associated with "cage breaking". This two movements are characterized by two different τ_c, as shown in Fig. 3.14.
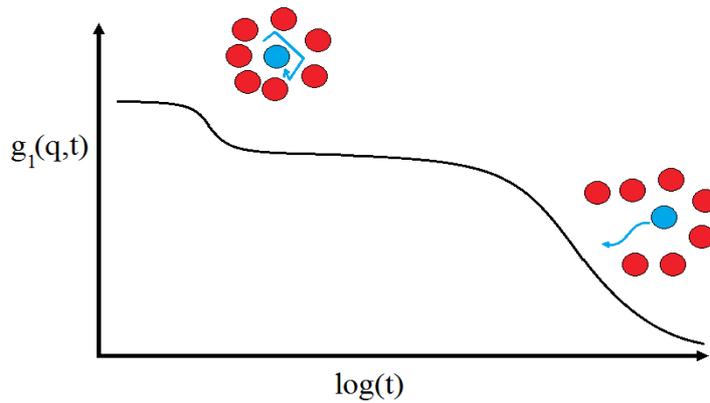
Figure 3.14: Typical intermediate scattering function for a supercooled liquid near the temperature T_G that brings it in the glass state. It shows the double decay typical of the two type of dynamics involved in the process

Approaching the glass transition, the viscosity of the system increases enormously and the particles need a longer time to escape their cages, giving rise to a much longer plateau in the intermediate scattering function.

To describe the nature of the process leading to the dynamical arrest in the glassy states, the PEL tackles the problem from the thermodynamic point of view (see Fig. 3.15): plotting the energy landscape described by the phase-space accessible by the liquid. During small relaxation times the system can only travel around the local minima, and to find the "true glass" minimum needs longer times, to access configurations that are further away in the phase-space.
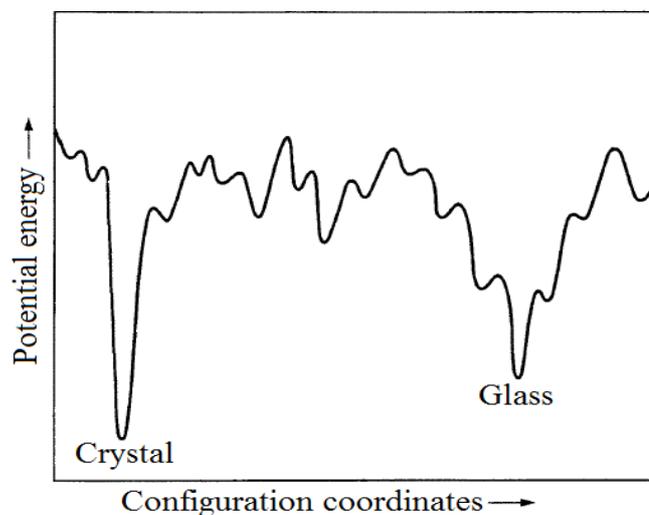
Figure 3.15: A schematic representation of a potential energy profile plotted in function of a generic coordinate in the phase space.

An example of the slowing down of the dynamics when a system approaches the glass transition is reported in Ref. [22] (as shown in Fig. 3.16), in the case of PMMA suspensions at high packing fractions were observed.
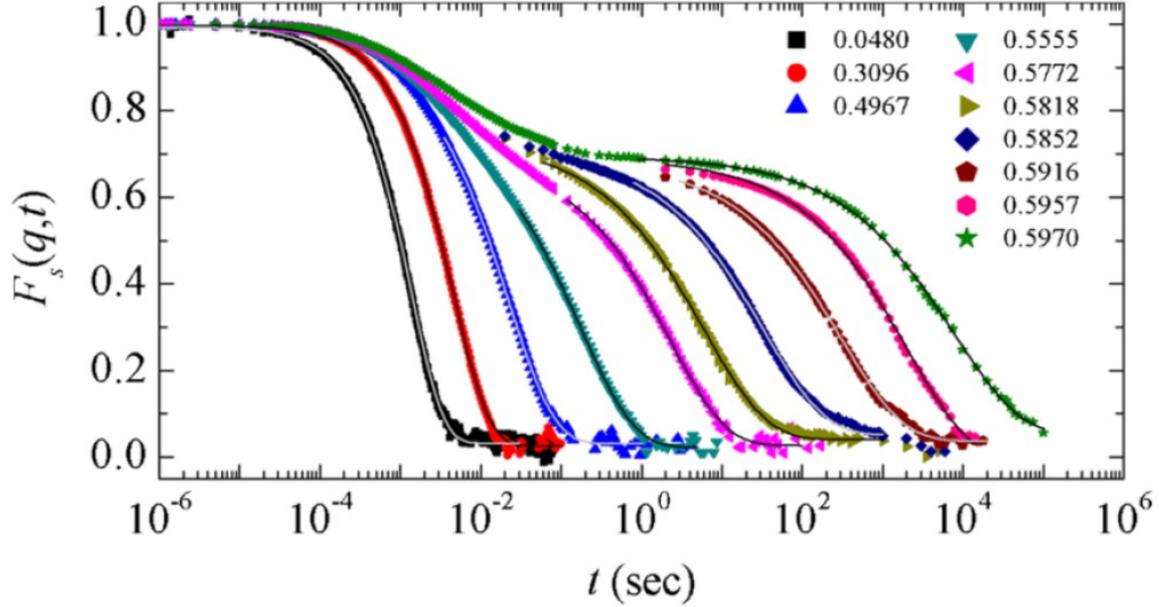
Figure 3.16: Intermediate Scattering function measured by DLS on high concentrated suspension of PMMA particles (R=260nm), as a function of different packing fraction. Taken by Ref. [22]

In this case (like many other arrested system like polymeric, gel or glassy one, characterized by soft or even weakly attractive interaction potentials) the correlation function typically assumes complex behaviours, and are usually empirically described by the Kohlrausch-Williams-Watts (KWW) function in the form:

$$g_2(\vec{q}, t) \;=\; 1 + \beta \exp\left[-2\left(t/\tau\right)^\gamma\right] \;.\tag{28}$$

The exponent γ is the *shape* parameter. We have seen that a value of $\gamma = 1$ is typical of Brownian motion (as shown with eq. 27), while this system assumes values $\gamma < 1$, which correspond *stretched exponential* behaviour.

Two different approaches could describe these observed deviations from the simple exponential decay: the spatially dynamical homogeneous scenario, and the heterogeneous one. In general, any correlation function can be cast into form of superposition of exponentials with some appropriate probability density $\rho(\tau)$ for the relaxation times τ

$$g_2(t) \; = \; \int_0^\infty \rho(\tau) e^{-t/\tau} d\tau \; = \; \langle \exp(-t/\tau) \rangle \quad . \tag{29}$$

In this way, it is evident that there are many different ways of introducing a distribution of time scales which lead to the same deviation from simple exponential pattern, after averaging over the ensemble of the relaxing units, as schematically described in Fig. 3.17:
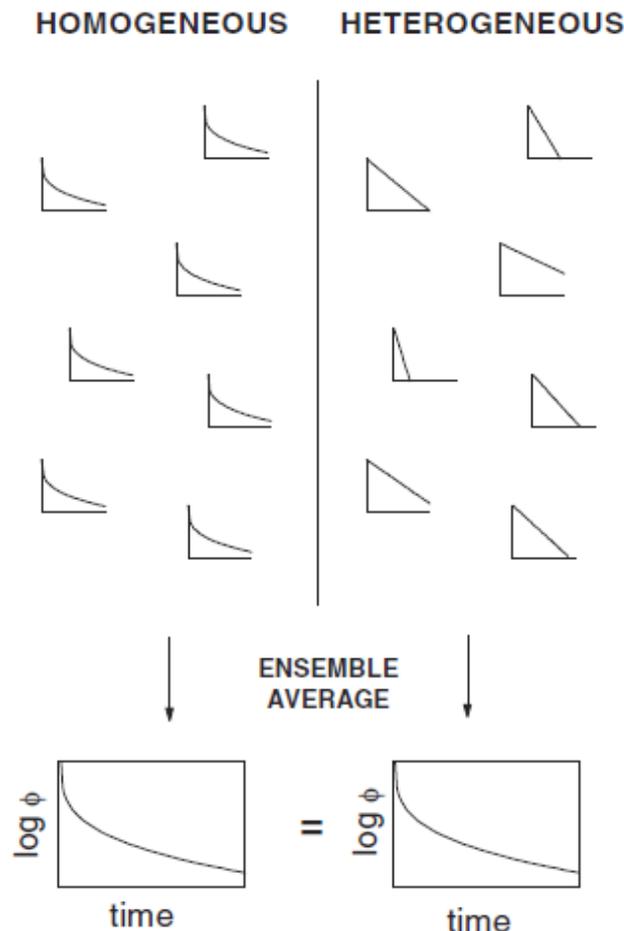
Figure 3.17: Schematic representation of two different sources of non-exponential correlation decays ([23])

In the left side, the "spatially homogeneous" scenario, the stretched behaviour is an intrinsic property of the system: each site within the sample contributes identically to the relaxation function, such that local and ensemble averaged dynamics are the same. In the other extreme, the "spatially heterogeneous" approach on the right side of Fig. 3.17, every region in the system is characterized by purely exponential dynamics, but whose relaxation times τ varies both in space ad time. Averaging over all the different region gives rise to

the stretched behaviour of the ensemble. In the last years, several simulations and experiments have directly established that the dynamical slowing down encountered in glassy materials is accompanied by the existence of a growing correlation length scale over which local dynamics is spatially correlated, the so called cooperatively rearranging regions introduced in [15], hence supporting supporting the heterogeneous scenario ([24]).

3.2.2.3 Dynamics of complex disordered systems: compressed exponential function

Differently from the above mentioned two systems, in some complex materials the slowing down of the dynamics can be described by a faster than exponential decay. In this case the intermediate scattering function can always be described by Eq. 28 but with a shape exponent γ larger than one. This is the case for instance of different gels, polymers, metallic glasses, nanoemulsions, etc. (Refs. [9], [25], [26] or [27], [28], [29]).

To account for *compressed exponential* behaviour (Eq. 28 with $\gamma > 1$), the model author by J.-P. Bouchaud and E. Pitard ([30]) computes the dynamical structure factor of an elastic medium characterized by random micro-collapses that appear at random in space and time, generating force dipoles that rearrange the local structure. This model suits the needs of an ideal elastic colloidal gel sample, where the particles aggregate when they come near enough one to each other, generating a field of mechanical stresses.

The model predicts that the correlation functions of the system decay as a compressed exponential with a shape factor $\gamma = 1,5$, when the relaxation time is much faster than the time scales of the collapses. This value for the compression exponent is accompanied by a inverse proportionality of the relaxation time in respect to the exchanged momentum ($\propto q^{-1}$), while the Brownian motion is characterized by a τ proportional to q^{-2} .

3.2.3 Ageing systems: the two-time correlation function

Many systems (complex soft materials glasses...) are characterized by history dependant properties. In this case their dynamics is not stationary, and the system will display physical ageing: this means that any physical observable will evolve with waiting time or sample age.

In this case the temporal average employed in calculation of $g_2(\vec{q}, t)$ could mask this kind of variation, instead a good description should contains information on how the dynamic changes through time.

The temporal evolution of the dynamics can be directly captured by XPCS calculating the so called *two-times correlation function*:

$$G(\vec{q}, t_{1,} t_2) = \frac{\langle I(\vec{q}, t_1) I(\vec{q}, t_2) \rangle_V}{\langle I(q, t_1) \rangle_V \langle I(q, t_2) \rangle_V} \tag{30}$$

where subscript V indicates averaging over the scattering volume. The result is a function of two temporal values, usually represented in a 2D graph such as the one reported in Fig. 3.18.
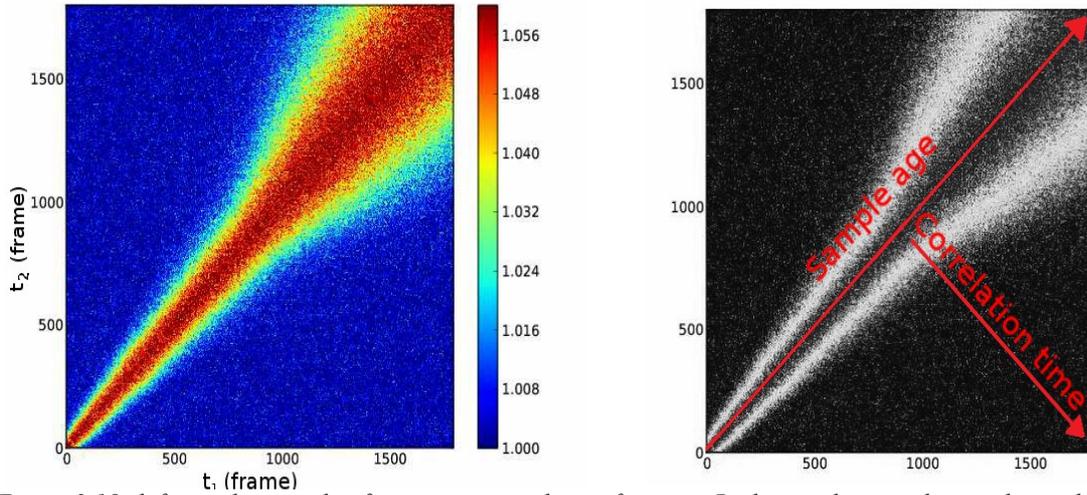
Figure 3.18: left panel, example of two-times correlation function. Right panel: same data with simple indications to read the graph: ([31])

This function represents the instantaneous correlation between two times t_1 and t_2 and it is a time-resolved version of the $g_2(\vec{q}, t)$. It has his maximum along the low-left / up-right diagonal (where $t_1 = t_2$ increases), representing the $I(\vec{q}, 0)$ as a function of the sample age thorough the measurement. For every point of the diagonal, the decaying values along the perpendicular direction (following the time delay $\Delta t = t_2 - t_1$) gives the "instantaneous" correlation function at a given age.

If the dynamics is stationary, or the changes due to ageing are slower with respect to the time interval $\Delta t = t_2 - t_1$ chosen, then the $g_2(\vec{q}, t)$ can be retrieved averaging the $G(\vec{q}, t_{1,} t_2)$ in this fixed time delay :

$$g_2(\vec{q}, t) = \langle G(\vec{q}, t_{1,} \Delta t) \rangle_{\Delta t} \tag{31}$$
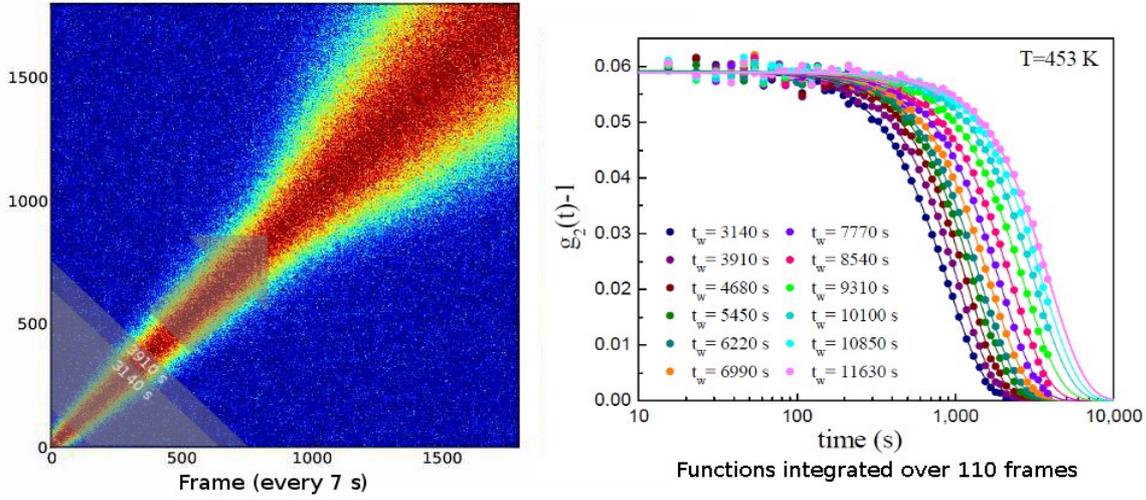
Figure 3.19: left panel: two times correlation function with two different time intervals highlighted. The arrow hint at the other series reported in the right panel but not highlighted Right panel: correlation functions calculated over several different time intervals.

On the left side of Fig. 3.19 is represented an example of a two time correlation function measured by us in the case of a $Pd_{77}Si1_{6.5}Cu_{6.5}$ metallic glass at 180°C. The shaded areas indicates the first two regions where $g_2(\vec{q}, t)$ is calculated using eq. 31: the centre of the area is the age t_1 of the sample at which we are evaluating the instantaneous correlation. The wideness of every area along the diagonal is the $\Delta t = t_2 - t_1$ along which the function is averaged: larger Δt means better statistic, but less specific information. It is important to select a range for the average in which the dynamic is consistent.

The two-times correlation functions can give many informations on a glance, as shown in the two literature examples in Fig. 3.20: the figure on the left is taken from Ref. [27] . The system investigated in the article was a chemically cross-linked resorcinol-formaldehyde (RF) polymer gel. Gel system usually shows very complicated structures, depending on temperature, solvent condition, molar ratio of the chemical, reaction time, etc. The figure is used to show that in a 10 minutes window, the dynamics of the system is stable and the g_2 can be time-averaged over ~10 minutes without loss of information.
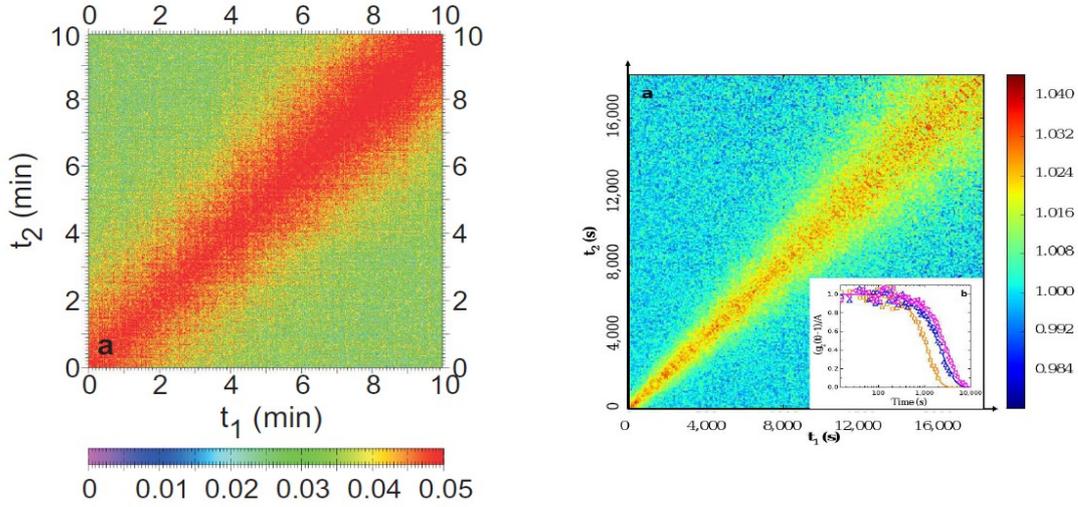
Figure 3.20: examples of two times correlation functions. On the left: An resorcinol-formaldehyde polymer gel taken from Ref. [27] . The contours parallel to the diagonal shows that the dynamics is not changing over the 10 min interval. On the right: Ageing in a out of equilibrium metallic ($Mg_{65}Cu_{25}Y_{10}$) glass at T=318°K, from Ref. [25] . a)Two times correlation function, the broadening of the red-yellow ridge shows the slowing down of the dynamics. Inset b) from left to right $g_2(\vec{q},t)$ functions for different sample ages at 4680 s, 9840 s and 12960 s

Instead the right plot, took from Ref. [25] , shows a metallic glass ($Mg_{65}Cu_{25}Y_{10}$). The system is prepared melting the metals to the liquid states, and then cooling them down at extremely high rate (10^6 °K/s) from the melting point to room temperature . The sample is then measured at different temperatures, showing dynamics that depends not only from the current state but also from the history of the sample (past temperatures, cooling/heating rates, etc...). This specific plot is relative to a two times correlation function taken after bringing the sample up in temperature. The system starts to relax the internal stresses "frozen" by the rapid quench, and moves towards a configurations characterized by slower dynamic. $g_2(\vec{q},t)$ functions can then be time averaged for better statistics (as in 3.20 (b)), integrating on time lapse small enough that the "rift" along the diagonal keeps the same width.

In many systems the ageing is usually accompanied by the presence of temporal hetero-geneity. These fluctuations in $G(\vec{q},t_1,t)$, ca be measured by the normalized variance ([32], [33]):

$$\chi(\vec{q},t)=\frac{\langle G(\vec{q},t_1,t)\rangle_{t_1}-\langle G(\vec{q},t_1,t)\rangle_{t_1}^2}{(g_2(\vec{q},0)-1)^2} \tag{32}$$

As an example, see Fig. 3.21: the broad maximum at around 0.5-1 s is a consistent hint of dynamical heterogeneity in this time scale .
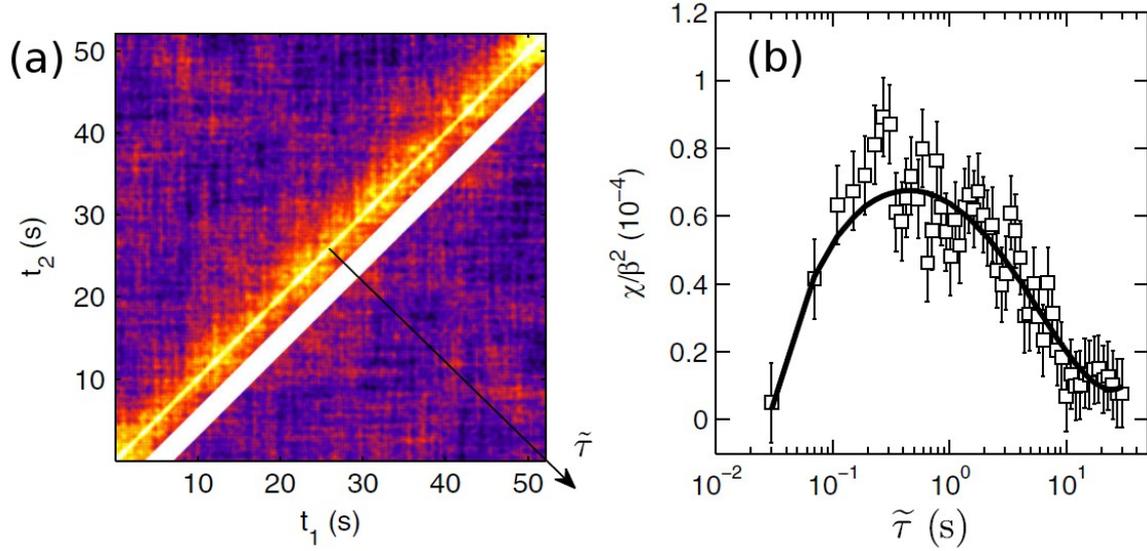
Figure 3.21: Two times correlation function for a 7nm gold nanoparticles film, suspended at the air-water interface. The (a) inset on the left shows the two times correlation function, and the white band is a guide to the eye that shows the range over which the variance is calculated. The inset (b) shows the total variance χ of the $G(\vec{q}, t_1, t)$ ([9]).

If the variance analysis suggests some time that can have meaningful variation, the four times correlation function $g_4(\vec{q}, t, \tilde{\tau})$ can be calculated, defined as

$$
\begin{aligned}
g_4(\vec{q}, t, \tilde{\tau}) &= \langle C(t_1, t_1+\tilde{\tau}) C(t_1, t_1+t, t_1+t+\tilde{\tau}) \rangle_{t_1} \\
&= \langle I(t_1) I(t_1+\tilde{\tau}) I(t_1+t) I(t_1+t+\tilde{\tau}) \rangle_{t_1}
\end{aligned}
\tag{33}
$$

The first lag time $\tilde{\tau} = |t_1 - t_2|$, (in Fig. 3.21 indicated by the lighter stripe) indicates the selected subdiagonal of the $G(\vec{q}, t_1, t)$ along which $g_4(\vec{q}, t, \tilde{\tau})$ is calculated. The second lag time, t , corresponds to the separation between two instants of the selected diagonal. Averages are performed over the initial time t_1 . This quantity gives information on the periodicities of the temporal heterogeneities.

4 The experiment

The XPCS measurements were executed at the soft interfaces and coherent scattering beamline ID10 at the European Synchrotron Radiation Facility (E.S.R:F.) in Grenoble, France in grazing angle geometry: the sample was placed in a Langmuir trough, and a monochromatic X-ray beam with a wavelenght of 1,55 Å (7,99 keV), 10x10 μm in size was directed towards the surface with an angle of 0,119°.

The scattered speckles were collected with a 2D Maxipix detector in the neighbourhood of the reflected beam from the surface, covering a $\vec{q}$ range from 0,001 to 0,004 Å^{-1}.

4.1 Beam shaping: the ID10 beamline at ESRF

A schematic representation of the ID10 beamline at ESRF, is shown in Fig. 4.1
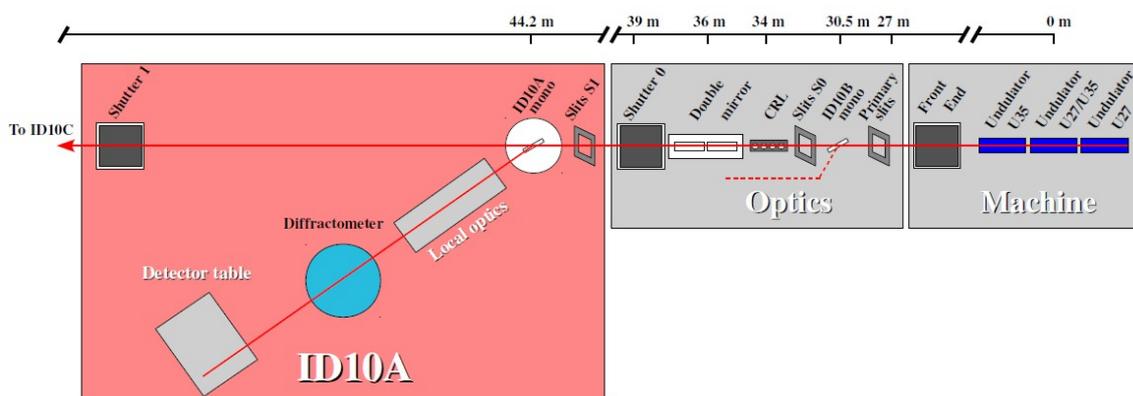

Figure 4.1: Schematic representation of the ID10A beamline with typical element distances.

The X-ray beam is generated when the electrons in the storage ring pass through the undulators. The source size is then defined by a primary and a secondary sets of slits, placed

respectively 27 m and 33 m from the undulators source. Reducing the effective source size increases transverse coherence length ξ_T.

A set of Beryllium Compound Refractive Lenses (CRL), located 34 m from the source is used to focus the beam at the sample position (46 m). This element is followed by another set of slits that cuts higher harmonic radiation: since the focal distance decrease with λ, the high energies photons are less collimated, and a good portion of them can be removed by the slits (see Fig. 4.2), providing a first selection in energy and reducing the heat load on the subsequent optics elements.
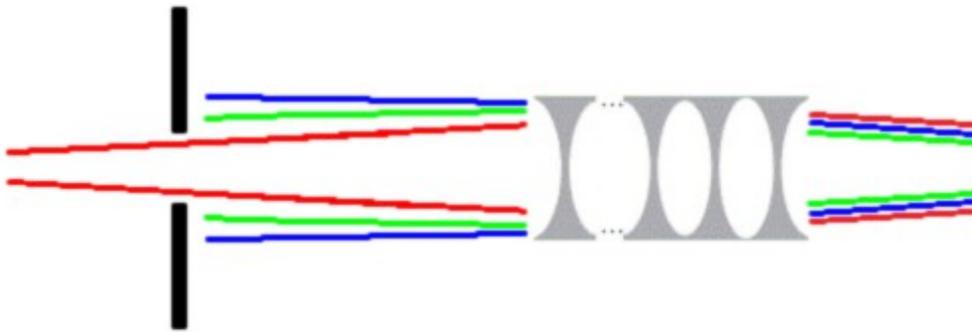
Figure 4.2: The focus of the CRLs depends on the incoming energy. As the energy of the photons increases (shown in false colours from red, lower energy, through green to blue, higher energy) the lenses focus the beam further. A slit placed just after the CRL can be used to stop higher harmonics generated from the undulator, and reduce the heat load on the monochromator.

A single-bounce Si crystal monochromator, placed 44.2 m downstream allows to tune the longitudinal coherence length (see Eq. 8) by selecting a monochromatic beam. The local optics, present in the experimental hutch downstream of the monochromator, include a double Si mirror to suppress higher order reflections (since the critical angle is different). A set of highly polished high-precision slits with cylindrical edges, placed just upstream of the sample, at 45.5 m, defines the final beam size. With the partially coherent beam, these slits produce a parasitic scattering pattern, which can be removed by placing guard slits just a few centimetres before the sample.

4.1.1 Undulators

An undulator is an insertion device, inserted in the Synchrotron storage ring. It consists of two rails with a series of magnets, with alternating polarity, designed to make the electrons oscillate back and forth. At each oscillation the electrons emit radiation.
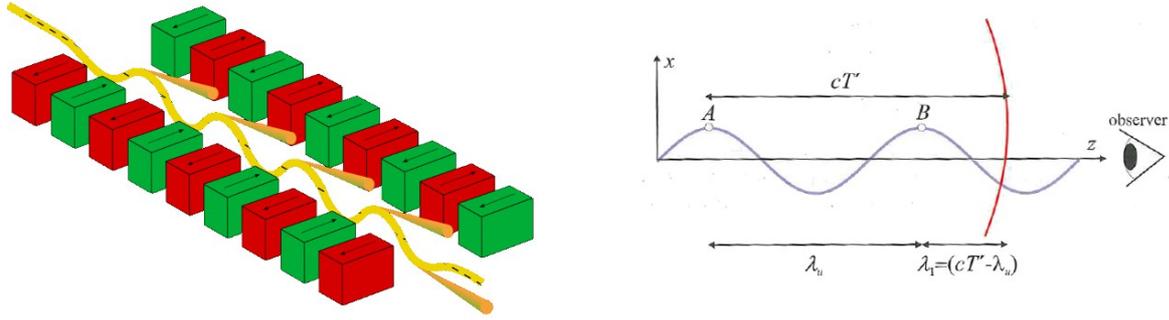
*Figure 4.3: on the left a scheme of the undulator, with in red and green the two series of alternating magnets, and in yellow the trajectory followed by the passing electron and the small cones representing the emitted radiation. On the right the radiation seen by a on-axis observer, result of the interference of the waves emitted at each crest of the trajectory.*

The magnets in the undulator are spaced in a way that all the emitted radiation with a given wavelenght interfere coherently at the end of the undulator. This schematically shown in the right panel of Fig 4.3. Consider the wave emitted by the electron in point A. After a time T' the electron is in point B and emits again. At this moment the wave emitted in A is already in position cT'. The idea is setting the velocity of the electrons and the magnetic field emitted by the undulator so that the waves of wavelength λ emitted in subsequent oscillations interfere constructively.

The condition for coherence is that the distance $cT' - \lambda_u$ equals one wavelenght λ (or a multiple thereof), being λ_u the period of the magnets inside the undulator.

When this conditions are fulfilled, also the divergence of the power emitted decreases, as the wavelength that carries the most power (λ) do not interfere constructively when observed off-axis.

The parameter T' can be modified by changing the distance between the two magnetic rails, in oredr to vary the strength of the magnetic field generated by the magnets: somewhat counter-intuitively a larger field produces a softer X-ray fundamental (larger values of λ correspond to less energy per photon).

The undulators have a number of advantages over sources that use only the effect of the magnetic field on the electron to generate X-ray (for example bending magnets and wigglers). As the emitted radiation has a narrower spectrum centred on the used wavelength, or the the heat load on the subsequent optics elements will be lower in respect of another kind of source of the same power, or, at least, it will all be due to useful radiation.

A detailed review of the device, with a derivation of this results can be found in Ref. [12] or Ref. [34].

4.2 Sample placing / Air-water interface measurements
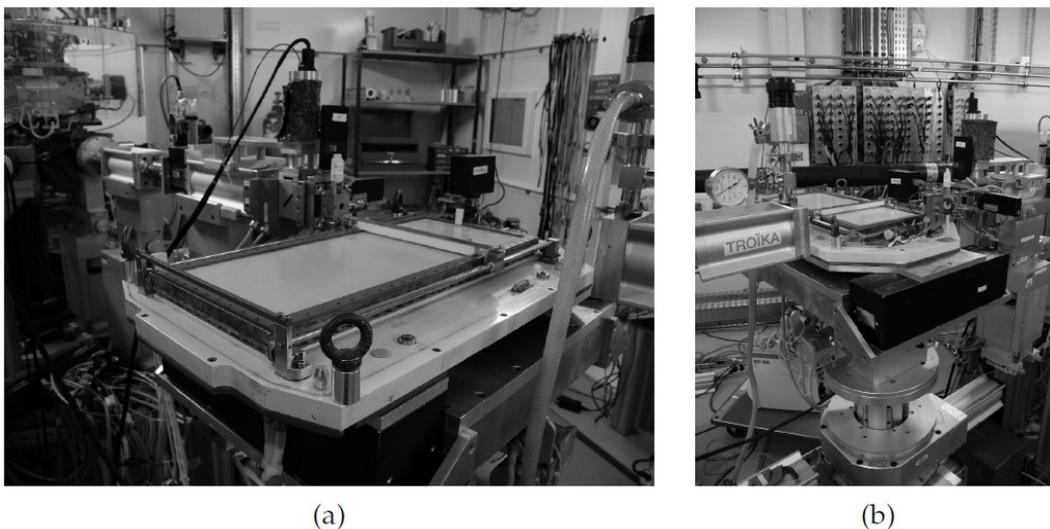
Figure 4.4: Photos of the Langmuir trough used for the XPCS measurements at the air/water interface.

A Langmuir trough was mounted on the spectrometer (see Fig. 4.4), mechanically isolated from the rest of the system via an anti-vibration table. The Langmuir trough has a single teflon barrier, and it is controlled by R&K3 hardware. The total area can be varied in the range 106 - 687 cm^2. The dimensions of the trough are dictated in order to minimize meniscus-related effects, and this limits the reachable compression ratio. The Langmuir setup includes also a Wilhelmy balance, manufactured by NIMA.

The whole setup is covered by a plexiglass cap equipped with Kapton windows in the beam path, and helium is continuously flushed in the chamber, to provide a controlled atmosphere that limits both parasitic scattering and radiation damage on the sample.

4.3 Detector

The scattering from the sample was collected with a 2D MAXIPIX detector, consisting of a matrix of 256x256 square pixels each one of 55x55 μm ([35]), and located 2050 mm far from the sample. This geometry corresponds to a covered $\vec{q}$ range between 0,005 and 0,2 nm^{-1}.

The diffraction pattern arising from the Langmuir film is anisotropic, hence for the analysis the pixels have been grouped into square sections. As indicated in Fig. 4.5 each of

them is identified by two components of the exchanged momentum, $q_\perp$ and $q_\parallel$, perpendicular parallel respectively to the water surface.
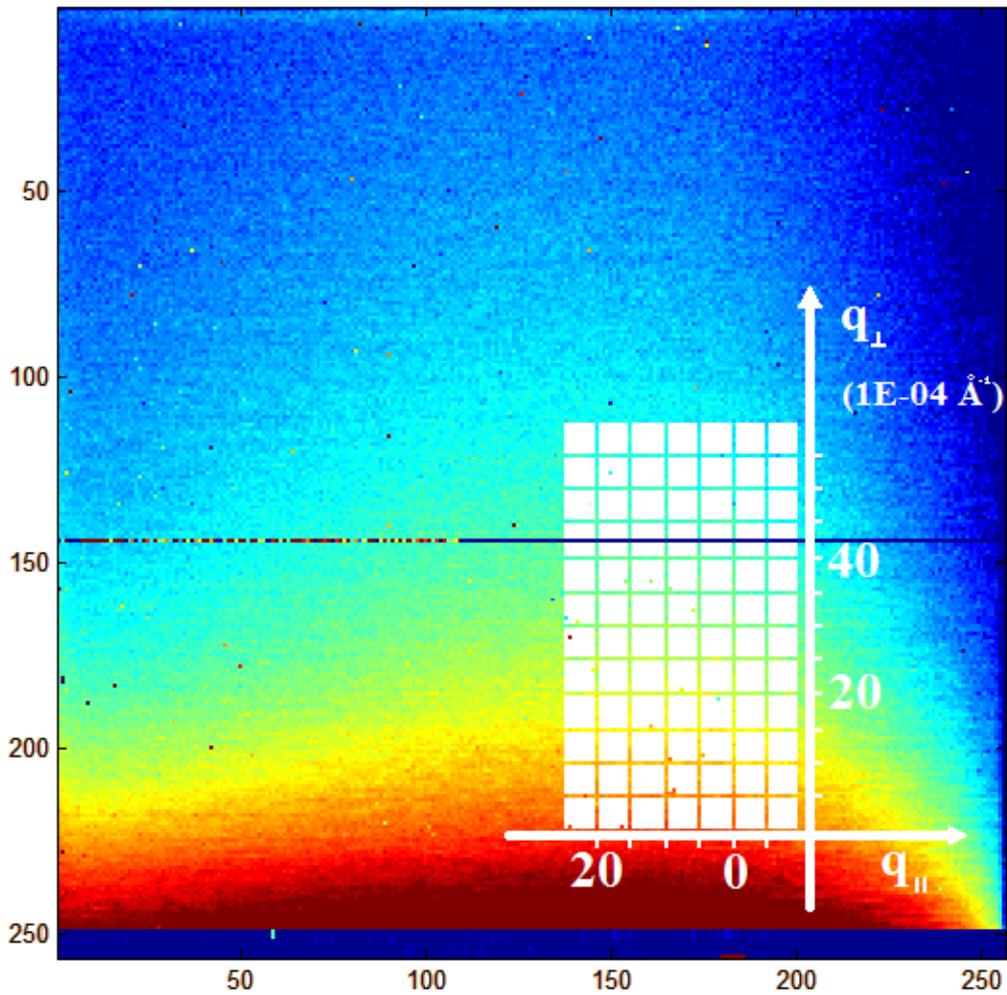
Figure 4.5: Measured diffraction pattern of the 2D film, with superimposed the mask used for the analysis. The missing pixels in the mask have been automatically excluded.

4.4   Measurements protocol

During the measurement the footprint of the X-ray beam on the sample surface was of 10 μm x 4,7 mm .

In order to avoid radiation damages on the film ad to explore different sample positios, the illuminated region was moved after every measurement by moving the trough.

Several series of data were collected at different pressures between 8 and 14 mN/m, taking sets of 10.000 images, at 100 ms interval between each other.t

5 Results and discussions

5.1 Data analysis

5.1.1 The two-times correlation function

As discussed in chapter 3.2.3, the dynamics of out of equilibrium system can vary greatly during the time employed for the measurements. This effect can be achieved by looking at the two-times correlation function $G(t_1, t_2)$.

We checked the presence of ageing in the sample in the investigated time frame, in order to decide for how long we can consider the dynamics stationary and to find a meaningful time interval for the calculation of the autocorrelation function $g_2(\vec{q}, t)$.

An example is reported in Fig. 5.1 for the $G(t_1, t_2)$ function calculated at the smaller investigated $\vec{q}$ ($q_{\parallel} = 0.0045 \, \mathring{A}^{-1}$ and $q_{\perp} = 0,0005 \, \mathring{A}^{-1}$) at 12 mN/m, for the whole 1000 sec period (10.000 images, panel a). In the panel b,c and d, the $G(t_1, t_2)$ functions calculated in smaller intervals are reported as well. These last panels are thus equivalent to details around the main diagonal of the figure shown in panel a.
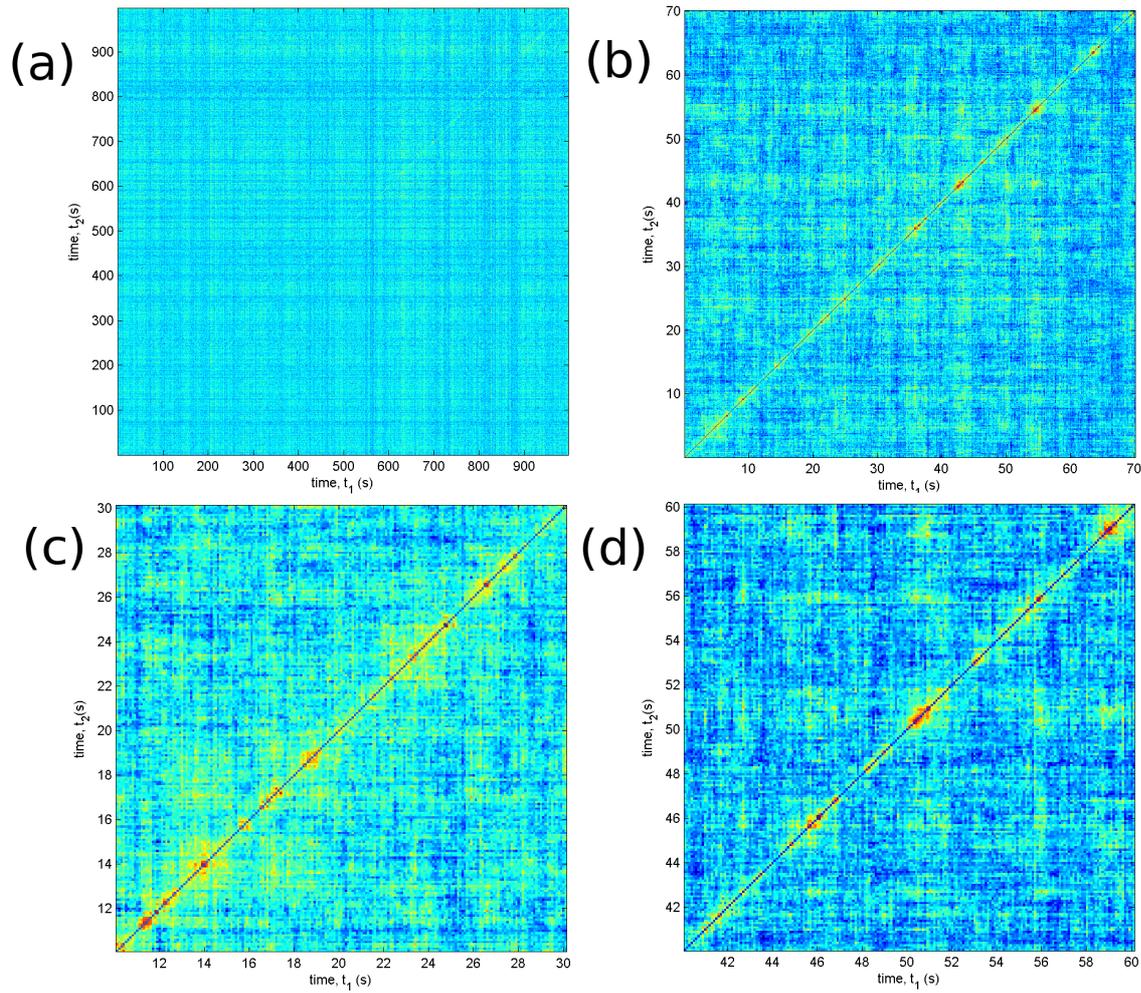
Figure 5.1: $G(\vec{q}, t_1, t_2)$ *measured for* $q_{\parallel} = 0.0045\, \overset{\circ}{A}^{-1}$ *and* $q_{\perp} = 0,0005\, \overset{\circ}{A}^{-1}$ *at* $\Pi = 12\ \mathrm{mN/m}$ *and different time intervals.*

In all the panels the scattered intensity gives rise to a thin yellowish line along the main diagonal. As explained in chapter 3.2.3, the broader the intensity in the two times correlation function, the slower the dynamics in the system. Hence, our data are a clear signature of fast dynamics. From the analysis of partial $G(\vec{q}, t_1, t_2)$ reported in panels *b,c,d*, it is evident that only random fluctuations occurs, and none consistent trend of ageing is evidenced in the investigated time scale. This means that integrating eq. 16 over long or short time windows will just enhance statistics without overlooking important details in the description of the dynamics.

In order to better understand the observed fluctuations in the $G(\vec{q}, t_1, t_2)$ we check the presence of temporal heterogeneities by calculating the corresponding variance χ of

$G(\vec{q}, t_1, t_2)$ (see chapter 3.2.3 for more details). Fig. 5.2 shows the temporal dependence corresponding variance χ, normalized by the contrast parameter obtained from the analysis of the intensity correlation function, as explained in the ext section.
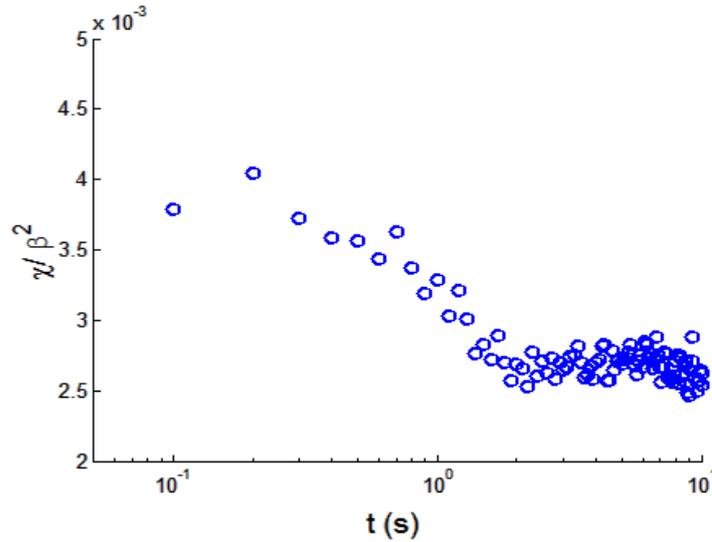
Figure 5.2: normalized variance of the two times correlation function reported in Fig. 5.1

A feeble peak might be observed at very short times. As will be shown later, this value is much shorter than the characteristic time τ of the autocorrelation functions. This result is not unexpected, as a similar peak has been already observed also in other colloidal systems ([9]). Unfortunately, given the small intensity of the peak, and the low temporal resolution, it is not meaningful to proceed to the analysis of the 4th order correlation function (see chapter 3.2.3).

5.1.2 Analysis of the correlation function

5.1.2.1 Fit strategy

Since the dynamics does not show any ageing in the period under scrutiny, we have proceeded to calculate the correlation function $g_2(\vec{q}, t)$ for the whole available range.

This relaxation dynamics (a example is reported in Fig.5.3) can be well described by the KWW function showed in eq. 28, which reads:

$$g_2(\vec{q}, t) = A + \beta \exp\left[-2(t/\tau)^y\right] \tag{34}$$

In simple terms the different parameters can be linked to different curve features:

- the *baseline* A is the long time limit of the correlation function;
- the *contrast* β characterizes the short time limit, and is related to the Siegert factor (eq. 22 and Ref. [10]) ;
- the *relaxation time* τ is to the time when the function reaches the value $A+0.13\beta$. Changing it results in an horizontal translation on the semi log plot.
- the *shape* γ is linked the angle of the tangent in the flex point (always in the in semilog plot).
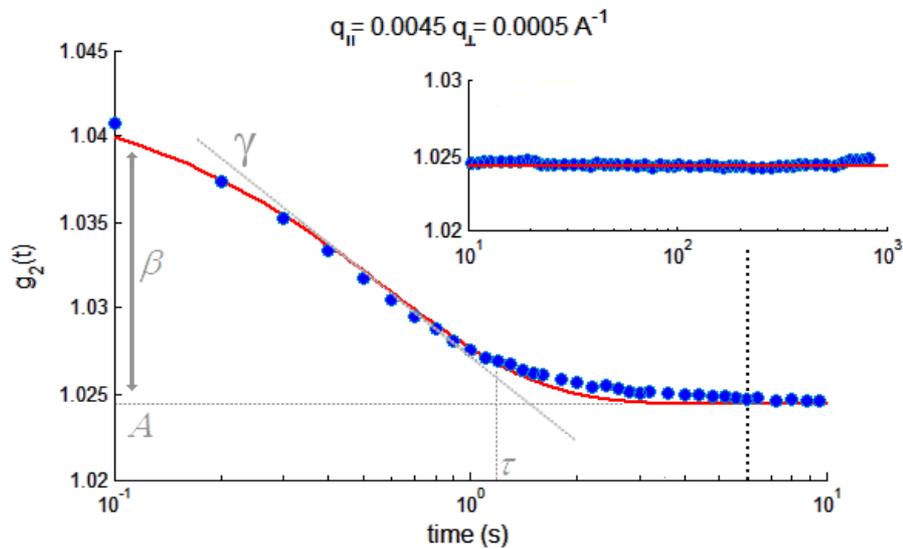
Figure 5.3: in blue the $g_2(\vec{q},t)$ *measured at* $\Pi=12\,\mathrm{mN/m}$ *, together with the best fit line which gives* $A=1,0244$ *,* $\beta=0,0185$ *,* $\tau=1,16$ s, $\gamma=1$ *. The inset shows the same function at longer times. The grey notes are a guide to the graphical meaning of the fit parameters.*

The parameter A , called also baseline, is the first parameter to be fitted: as it is clearly the value assumed by the function for $t\rightarrow\infty$, it is found evaluating the mean of the value of the function at long time (the part in the upper right inset in Fig. 5.5). As the correlation function is integrated on a finite time and the data are not continuous, as t increases every value of the correlation function is averaged over less pairs of points, so that the last points have always worse statistics than the first ones. That's why the last points are excluded to calculate A .

After A has been determined, the parameter is fixed and the other three parameters are fitted on the first part of the data (on the left side of the vertical black dashed line in

Fig. 5.3), so that the algorithm doesn't weight too much the less meaningful points on the right side, seen that their contribution is already been taken in account fixing A .

It is evident that the KWW can well reproduce our experimental data. Small deviations are observed in the tail of the decay. Similar behaviour have been reported for other complex soft materials and are signatures of a more complicate relaxation process at longer time scale, which consequently would require a much complex expression than eq. 34. Anyway the quality of the fit at shorter times shows how the KWW can still be used to reproduce the main part of the relaxation process.

5.1.3 The Shape properties

Table 1 reports the results of our data fits for the same $\vec{q}$ ($q_{\parallel}=0,0045\,\overset{\circ}{\mathrm{A}}{}^{-1}$, $q_{\perp}=0,0005\,\overset{\circ}{\mathrm{A}}{}^{-1}$) for different series with increasing ad decreasing surface pressure of the film:

- the first column lists the chronological order of the measurment;
- the second reports the pressure at which the measurements have been taken;
- the third, fourth and fifth show the results of the fit for the parameters indicated in title (shape γ , relaxation time τ and contrast β).

Series	Π (mN/m)	Shape γ	Relaxation Time - τ		Contrast - β	
			γ fitted	γ =1	γ fitted	γ =1
1	10	0,5 ±0,1	0,2 ±0,1	0,39 ±0,08	0,025 ± 0,03	0,011 ±0,005
2	12	0,9 ±0,1	0,81 ±0,05	0,83 ±0,05	0,025 ±0,003	0,024 ±0,005
3	14	0,7 ±0,1	1,1 ±0,1	1,26 ±0,10	0,019 ±0,003	0,015 ±0,002
4	12	0,7 ±0,1	1,3 ±0,1	1,38 ±0,11	0,024 ±0,002	0,019 ±0,002
5	10	0,7 ±0,1	0,8 ±0,05	0,91 ±0,08	0,034 ±0,006	0,027 ±0,003
6	12	0,6 ±0,1	0,5 ±0,05	0,67 ±0,07	0,035 ±0,007	0,023 ±0,005

Table 1: Comparison of fit results with parameter Shape fixed at 1 (grey columns) or kept free (white columns) for various surface pressures at the same $q_{\parallel} = 0,0045\,\overset{\circ}{\mathrm{A}}{}^{-1}, q_{\perp} = 0,0005\,\overset{\circ}{\mathrm{A}}{}^{-1}$

It is interesting to note that the shape of the decay results is always lower than one, leading to a stretched exponential behaviour ($\gamma<1$). As shown in the white columns of the table, both the shape parameter ad the contrast factor vary randomly upon changing the pressure. These fluctuations are probably related to the lack of a complete information on shorter times dynamics. Unfourtunatley, due to technical problems, we could not achieve

smaller time scale and get a better estimation for the shape parameter. For this reason, we analyse our correlation functions by keeping the shape γ fixed at $\gamma=1$: the corresponding results for τ and β are shown in the grey sub-columns in Tab. 1.

A comparison between the two different fitting procedures is show in Fig. 5.4 for different sets of data. It is clear that this procedure does not affect the values of the relaxation time, and so, for now on, we will discuss only results with the shape fixed at $\gamma=1$ if not stated otherwise.
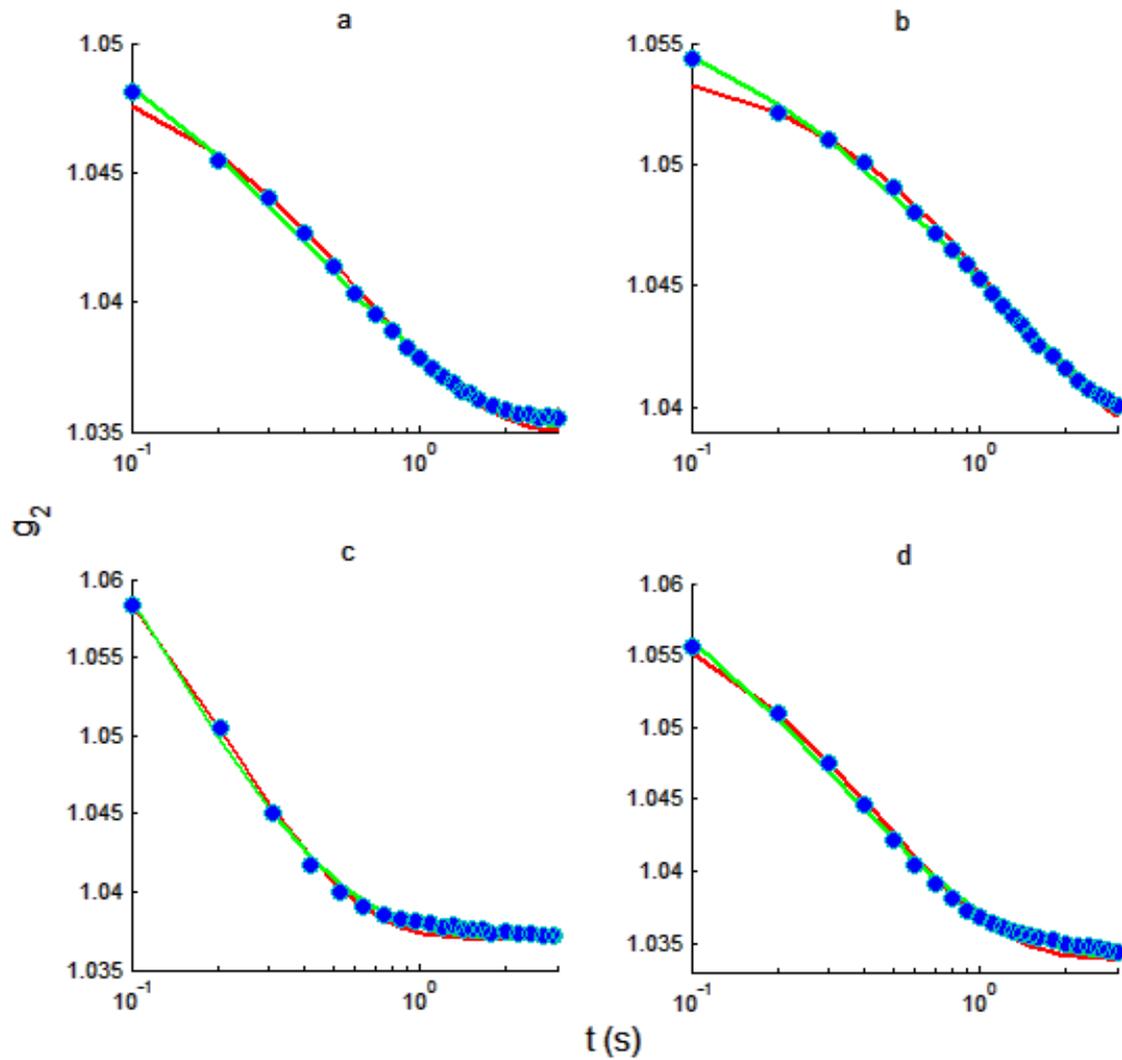
*Figure 5.4: Examples of data and fitted correlation functions for different pressures: the green curves show the fit with* γ *fitted, the red ones the results with* $\gamma=1$ *. The data are measured at* $q_{\parallel}=0{,}0045\ \mathring{A}^{-1}$ *and* $q_{\perp}=0{,}0005\ \mathring{A}^{-1}$ *at different pressure, (*a*) at* 12 mN/m, *(b) at* 14 mN/m, *(c) at* 10 mN/m *and (*d*) at* 12 *mN/m*

The shape parameter value can be taken as a signature of the interactions present in the system: as we have seen one expects $\gamma=1$ for Brownian motion while $\gamma=1.5$ is often found in colloidal gels [29].

5.2 Wavevector dependencies

From the analysis of the XPCS correlation functions, we get detailed information on the structural relaxation, and in particular we measured the characteristic time τ, which thus represents how fast the structure can rearrange itself to an equilibrium position. As we have seen in section 3.2.2 the dependence of this parameter from the wavevector at which is observed gives information on the nature of the dynamics present in the system. As an example, Fig.5.5 shows the values of τ as a function of the exchanged wavevector $\vec{q}$.
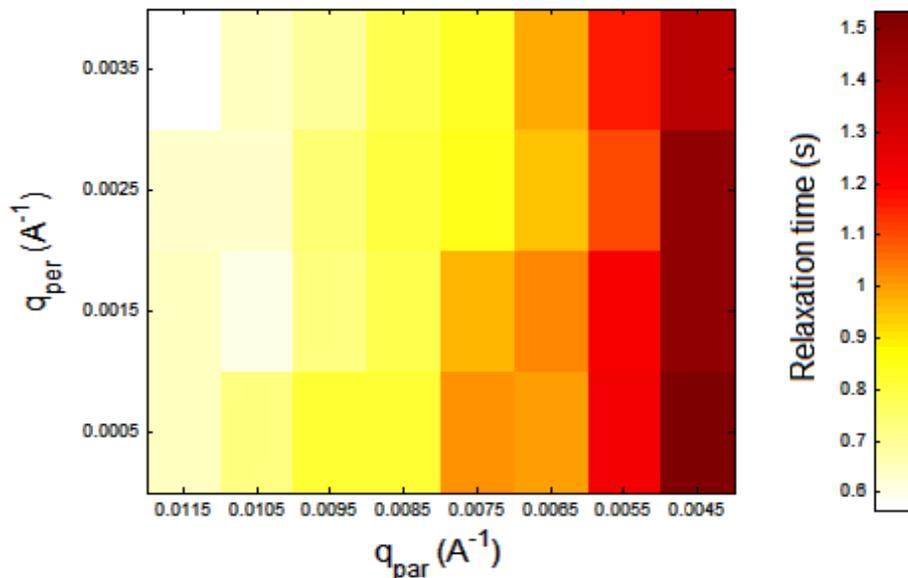
Figure 5.5: Values of the relaxation time τ in the reciprocal space , as a function of $\vec{q}$, measured at a surface pressure $\Pi=12\,\mathrm{mN/m}$.

5.2.1 Perpendicular wavevector

The first result is that within the experimental uncertainty there is no detectable dependency of the dynamics parameters from $q_\perp$ (see Fig. 5.5 for an example). This is natural for a 2D system. The lack of any $q_\perp$ dependence indicates that there is no motion per-

pendicular to the surface through the air-water interface, as it could be the case e.g. for collapsing 3D nanostructures.

5.2.2 Parallel wavevector

The dependence of the structural relaxation times from $q_\parallel$ is reported in Fig. 5.6 For the data measured at $\Pi = 12\,\mathrm{mN/m}$ after averaging over $q_\perp$ to improve the signal to noise ratio.
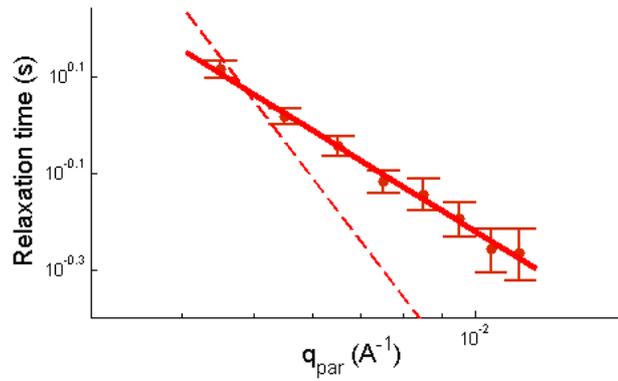

Figure 5.6: Relaxation times τ measured at different $\vec{q}_\parallel$ for $\Pi = 12\,\mathrm{mN/m}$. The fcorrespond to the best fit line obtained by using relation $\tau \propto q^N$, which gives a parameter $N = -0.94$. The dotted line shows the $\tau \propto q^{-2}$ dependence expected for Brownian diffusion.

The time τ strongly decreases as a function of the wavevector $q_\parallel$, and it can be well described by the power law:

$$\tau \propto q_\parallel{}^N \tag{35}$$

With $N \sim 1$. Similar $\tau \propto \dfrac{1}{q}$ dependence have been observed in many different arrested systems ([36]), such as oil nanoemulsion ([28]), colloidal polystyrene gels ([37]) and in molecular layers of polymers ([38]). In most of the cases however the correlation functions show compressed shapes ($\gamma > 1$ in the KWW expression) in disagreemet with our results. We recall that in our case the correlation functions have been fitted to a exponential decay ($\gamma = 1$ in the KWW expression, as discussed in section 5.1.3). This might suggest 2D Brownian diffusion. However, this hypothesis must be ruled out, as a Brownian diffu-

sion dictates a $\tau \propto q_{\parallel}^{-2}$ behaviour (dotted line on Fig. 5.6) in sharp contrast with our results.

To the best of our knowledge no detailed theoretical model is available which fits this situation and further investigation is required.

5.3 Surface pressure dependence

The system is not in thermodynamic equilibrium, hence variation in the avaible area A, and consequently of the surface pressure Π, can produce different effects depending on the history of the sample. A nice example of this was shown in the case of the isotherm cycle reported in the chapter 2.2.3 (Fig. 2.9).

In Fig. 5.7 we report the relaxation time as a function of the surface pressure Π at the wavevector $q_{\parallel}=0,0045\,\overset{\circ}{A}^{-1}$, $q_{\perp}=0,0005\,\overset{\circ}{A}^{-1}$. Similar trend has been observed for other $\vec{q}$. On increasing the pressure the dynamics slow down and τ evolve from 0.4 s at $\Pi=8\,\mathrm{mN/m}$ to $\sim 1.3\,\mathrm{mN/m}$: this effect can be rationalized in terms of free volume theories (in this case free area), more compacted particles are less mobile and display longer relaxation times. However this "natural" point of view cannot describe the behaviour observed upon reduction of surface pressure from 14 to 13 mN/m (from 4 to 5 in Fig. 5.7).In this case the structural relaxation time seems ot to be affected b the pressure changes: this is probably a sign that the previous compression triggered a reconfiguration of the system.
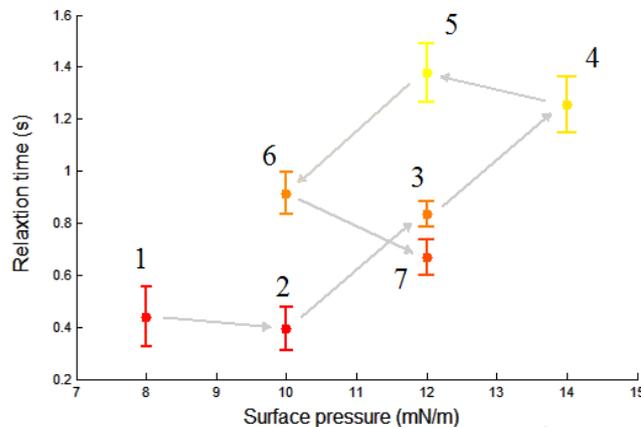
Figure 5.7: Showing relaxation time measured at $q_{\parallel}=0,0045\,\overset{\circ}{A}^{-1}$ *and* $q_{\perp}=0,0005\,\overset{\circ}{A}^{-1}$ *as a function of the surface pressure. The arrows show the order in the compression/decompression cycle.*

Further reduction of the pressure results in a slow loosening of the 2D film structure and hence an acceleration of its dynamics, which remains however slower than it was at the very same pressure before the compression (point 6 and 2 in Fig. 5.7). This is due to the irreversible character of the inter-particle interaction: when two particles come close enough to form a bond state they will remain linked even after the Π has been reduced.

If the film is compressed again from 10 to 12 mN/m (6 to 7) τ decreases, and the system reaches a similar situation as under the first compression procedure.

5.4 Comparison with the 7nm particles film

As it was discussed in chapter 2, our system has been prepared from an "older" version of the suspension already studied in Ref. [9]. In the "younger"sample, the nanoparticles were 7 nm in diameter and the film showed a more homogeneous morphology.

Fig 5.8 shows a comparison between the relaxation times observed at the same $\vec{q}$ range and for comparable values of surface pressure.
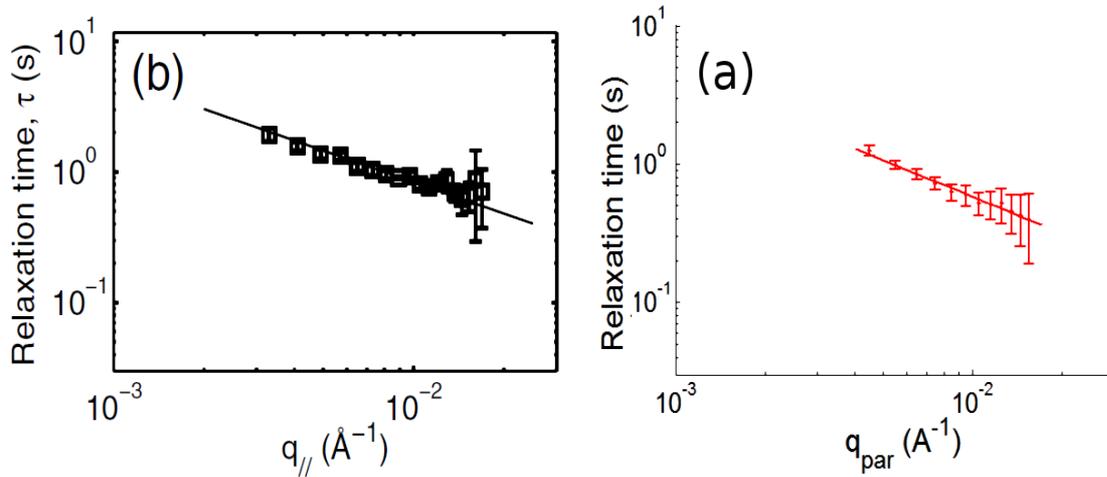
Figure 5.8: relaxation times τ *as a function of the paralell wavevector* $\vec{q}_{\parallel}$ *exchanged for the* 7 nm *(on the left) ad the* 80 nm *(on the right). The series on the left (taken from [9]) corresponds to a surface pressure of* 15 mN/m*., while the one on the right was taken during this experiment at* 14 mN/m*. Note how the* τ *values are comparable and the relation* $\tau = q_{\parallel}^{-1}$ *fits well both sets of data.*

In both cases τ is of the order of 1 s, and is inversely proportional to the parallel exchanged wavevector $q_{\parallel}$.

Differently from the dynamics observed in the 7 nm particles film, which shows faster than exponetial correlation function with a Shape parameter γ of 1.5, our $g_2(\vec{q}, t)$ can be described by a purely exponential shape.

We recall here that compressed shape is generally understood as a signature of internal stresses relaxation ([30]) which seems to be more important in the 7 nm particles film. The observed shape in our system can be interpreted has a consequence of the heterogeneity of the sample: the scattering volume comprehend very different regions, that are in all probability characterized by very different dynamics and relaxation times. The mean effect of a distribution of this kind is compatible with a stretched exponential.

6 Conclusions

In this Thesis work we have presented a detailed investigation of the dynamical properties of a Langmuir film of 80 nm gold nanoparticles, functionalized with dodecanethiol.

The internal dynamics of the system was measured by means of X ray photon correlation spectroscopy, on the mesoscopic spatial scale corresponding to tens/hundreds of nanometer, and for different surface pressure values.

We find that the dynamics is stationary in the time scale investigated by the measurement.

Small fluctuations in the intensity of the two times correlation function are observed, which could be related to the presence of fast temporal heterogeneities as suggested by the analysis of the variance of $G(\vec{q}, t_1, t_2)$. Unfortunately, a deeper investigation would require a better temporal resolution, which was not possible due to technical problems.

The dynamics of the spontaneous microscopic fluctuations can be well described by single exponential function, characterized by a structural relaxation time τ of the order of $\sim 1\,\mathrm{s}$.

A wavevector dependence study shows that the dynamics is confined to the surface of the film, as a consequence the structural relaxation time depends only on the parallel component of the wavevector $q_{\parallel}$. In particular we found that τ grows as the inverse of the exchanged momentum, $\tau \propto q_{\parallel}^{-1}$ for every investigate pressure.

Differently, an isothermal cycle of compression ad decompression, leads to an hysteresis in the structural relaxation times, which is likely due to the irreversible character if the intra-particle short rage attraction.

A comparison with a similar system with 7 nm nanoparticle, suggests the presence of a more heterogeneous dynamics on increasing the nanoparticles diameter, which is reflected on the more stretched shape of the intensity autocorrelation function.

It would be interesting to observe the system on a shorter time scale, and observe the evolution of the system for different intermediate nanoparticles dimensions.

7 Appendix A: Relaxation dynamics and ageing in metallic glasses

The behaviour of glass forming systems is broadly recognized as being rich in phenomenology both in the supercooled and in the glassy state. Despite of the large efforts done in the last decades, many aspects remain poorly understood and the understanding of the glassy state is still considered as one of the most challenging topics in condensed matter.

In general a glass can be viewed as a liquid in which a huge slowing down of the diffusive motion of the particles has destroyed its ability to flow remaining frozen in a metastable state, from which they slowly evolve or age towards the corresponding supercooled liquid phase. In fact the most common way to produce a glass consists on cooling a liquid fast enough to avoid crystallization.
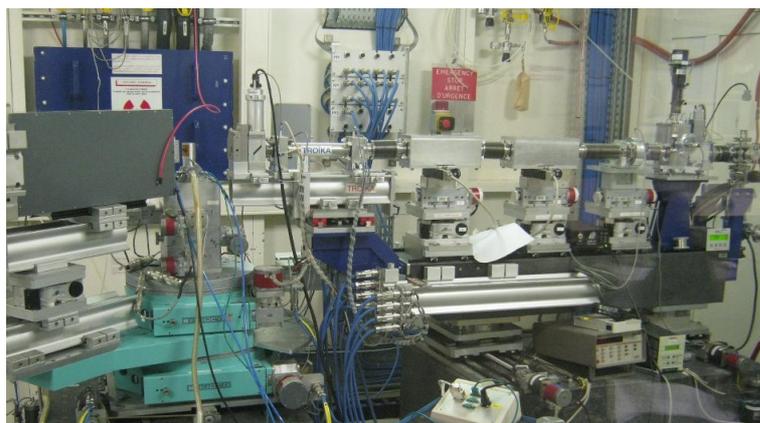

Figure 7.1: Photo of the setup used for the measurements

The scattered intensity was measured by an IkonM charge-coupled device (CCD) from Andor Technology which consists of 1024×1024 pixels, with 13×13 mm2 pixel size. The

transmitted scattered intensity was collected at a distance 0.68m from the sample and in a wide angle configuration, specifically at a scattering angle $2\theta = 40.6°$ with respect to the incident beam, as shown in Fig. 7.1.

In this way all pixels of the CCD were considered to belong to the same wave vector $\vec{q}_0 = 2.81 \mathring{A}^{-1}$, corresponding to the maximum of the static structure factor of the system, allowing us to investigate the dynamics at the inter particle distance of $2\pi/\vec{q}_0 \sim 2 \mathring{A}$. Focusing on the slow dynamics, we collected time series of up to about 2000 images with 7s exposure time per frame. The data were treated and analysed following the procedure described in Ref. [39].
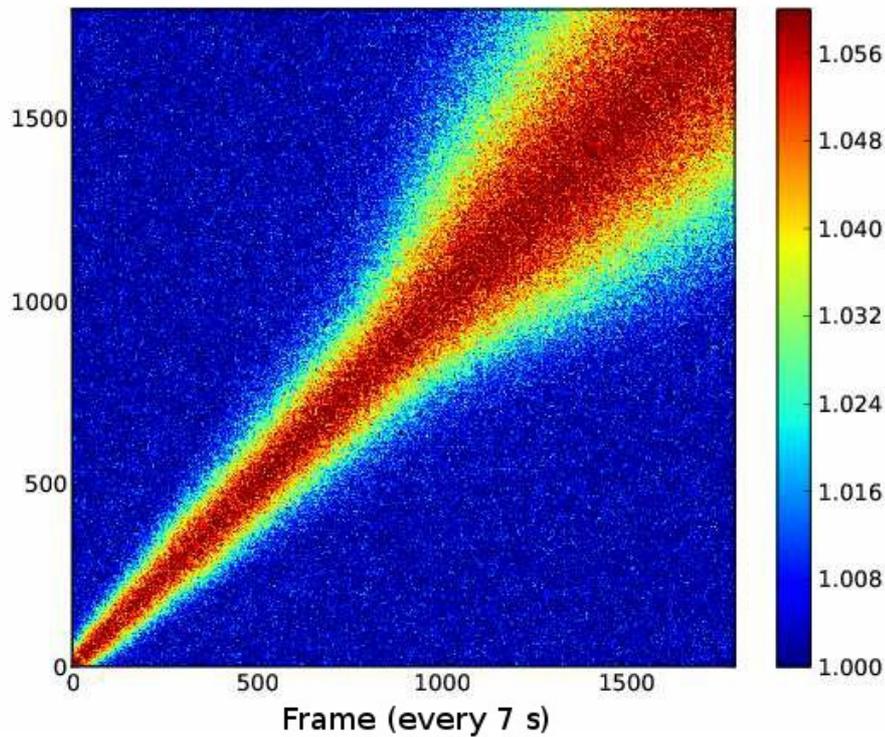
Figure 7.2: Two times correlation functions for $Pd_{77}Si_{16.5}Cu_{6.5}$, measured at $\vec{q}_0 = 2.81 \mathring{A}^{-1}$ and $T = 453K$.

Figure 7.2 shows the two times correlation function measured in $Pd_{77}Si_{16.5}Cu_{6.5}$ in the glassy state at T=453K. Differently from the 2D film investigated in this Thesis, here the dynamics is not stationary and the structural relaxation time increases with the sample age. The ageing is illustrated by the broadening of the diagonal contour as the sample age increase.

Although the dynamics is not stationary, the ageing is sufficiently slow that it is possible to find time intervals over which the $G(\vec{q}, t_1, t_2)$ can be averaged and thus to get the standard intensity autocorrelation functions which are reported in Fig 7.3 for different waiting time $\%t_w$ from temperature equilibration.
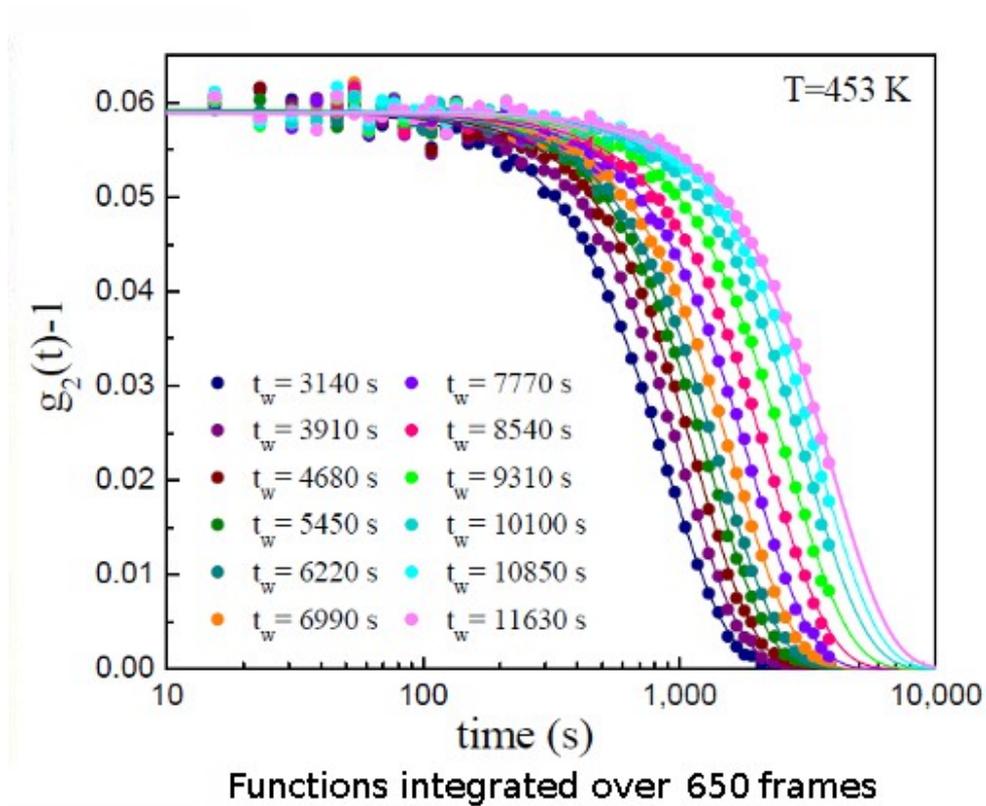

Figure 7.3: Intesity correlation functions for $Pd_{77}Si_{16.5}Cu_{6.5}$, measured at $\vec{q}_0 = 2.81\,\mathring{A}^{-1}$ and $T = 453K$, for different waiting times from temperature equilibration.

Here the dynamics is very slow, being τ in the order of thousands of seconds, and clearly shifts to longer values during the measurement. The data are here reported together with the best fit obtained by using the KWW function. Similarly to other metallic glasses ([25]) the shape parameter γ is found to be compressed ($\gamma > 1$) and independent from the sample age. This means that it is possible to rescale all the curves in one single master curve by reporting the data as a function of the time rescaled by the structural relaxation time obtained from the analysis of the data, as shown in Fig. 7.4.
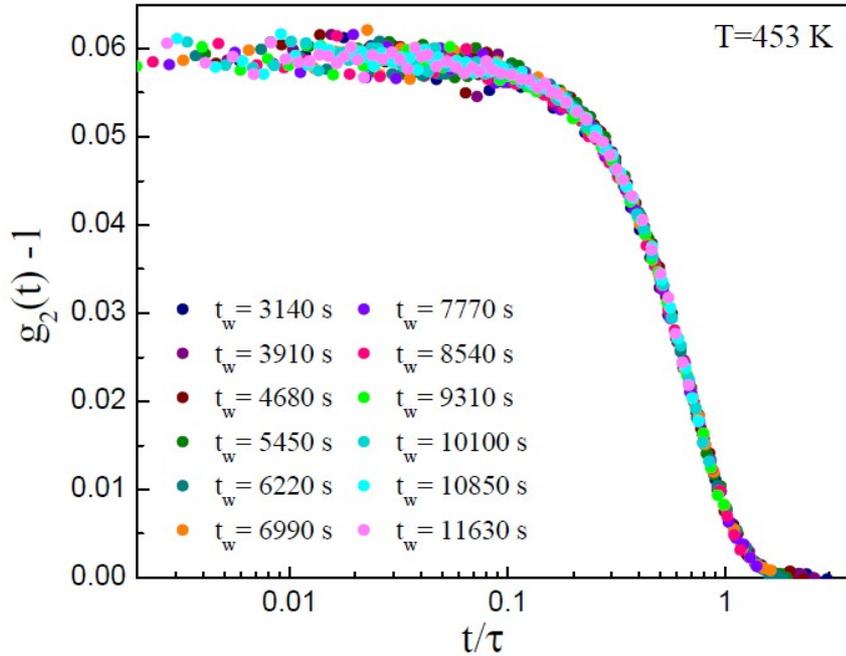
Figure 7.4: Same data as in Fig. 7.3 reported rescaled as a function of t/τ .

The Fig. 7.5 shows the structural relaxation times as a function of the waiting time for all the reported correlation functions: τ clearly grows up exponentially and can be well described by the empirical function

$$\tau(T,t_w)=\tau_0(T)\exp(t_w/\tau^*) \quad . \tag{36}$$
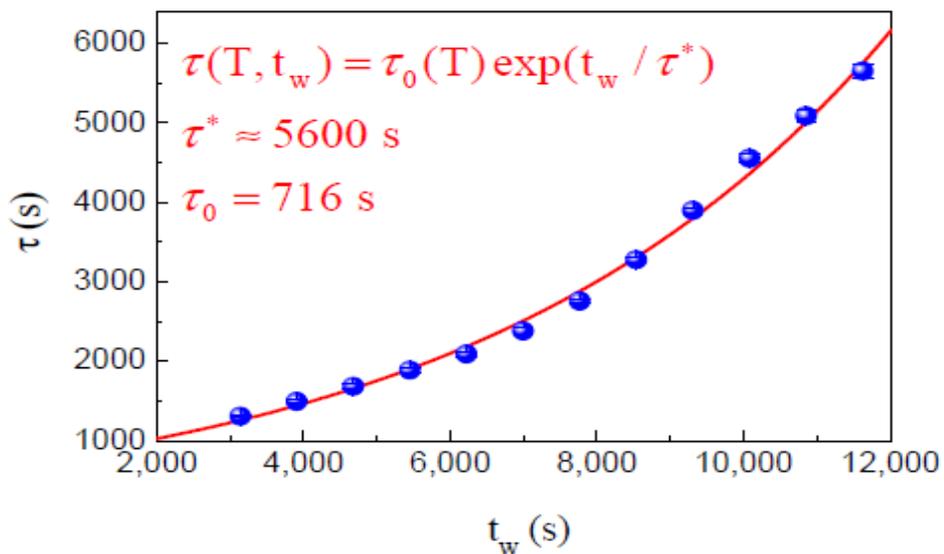
Figure 7.5: Waiting time dependence of the structural relaxation time. The red line is the best fit obtained with eq. 36

In this expression, τ_0 is the starting value of the structural relaxation time and depends on the temperature T, and τ^* describe the rate of ageing.

We find $\tau^* \sim 5000s$ in agreement with the values reported for other metallic glasses ([25]). As in those cases this fast ageing regime is likely to be related to the release of internal stresses stored in the system during the fast quenching used to produce the glass.

8 Bibliography

[1]   **V. M. Kaganer, H. Mohwald, P.Dutta (1999)**. *Structure and phase transitions in Langmuir monolayers*. In *Reviews of Modern Physics*, **71**, p. 779-819.

[2]   **M. Brust, M. Walker, D. Bethell, D. J. Schiffrin, R.n Whyman (1994)**. *Synthesis of Thiol-derivatised Gold Nanoparticles in a Two-phase Liquid-Liquid System*. In *Journal of the Chemical Society, Chemical Communications*, **7**, p. 801-802.

[3]   **S. Chen, K. Kimura (1999)**. *Synthesis and Characterization of Carboxylate-Modified Gold Nanoparticle Powders Dispersible in Water*. In *Langmuir*, **15**, p. 1075-1082.

[4]   **D.Orsi** (**2011**). *Dynamical and Rheological Characterization of 2D Architectures at the Air/Water Interface*. Ph.D. thesis, Università degli Studi di Parma.

[5]   **W. Haiss, Nguyen T. K. Thanh, J. Aveyard, David G. Fernig (2007)**. *Determination of Size and Concentration of Gold Nanoparticles from UV-Vis Spectra*. In *Analytical Chemistry*, **79**, p. 4215-4221.

[6]   **Roberts,** (**1990**), *Langmuir-blodgett films. Vol. 1*. Gareth Gwyn (Ed.), New York: Plenum press.

[7]   **A. Pockels (1891)**. *Surface Tension*. In *Nature*, **43**, p. 437-439.

[8]   **D. Orsi, G. Baldi, P. Cicuta, L. Cristofolini (2012)**. *On the relation between hierarchical morphology and mechanical properties of a colloidal 2D gel system*. In *Colloids and Surfaces, A: Physicochemical and Engineering Aspects*, **413**, p. 71-77.

[9]   **D. Orsi, L. Cristofolini, G. Baldi, A. Madsen (2012)**. *Heterogeneous and Anisotropic Dynamics of a 2D Gel*. In *Physical Review Letters*, **108**, p. 105701.

[10]   **B. J. Berne, R. Pecora** (**2000**), *Dynamic Light Scattering, with applications to chemistry, biology, and physics*. (Ed.), Dover Publications Inc..

[11]   **G. Grübel, A. Madsen, A. Robert** (**2008**). X-Ray Photon Correlation Spectroscopy (XPCS). }(Ed.), *Soft-Matter Characterization*, Springer.

[12]   **J. Nielsen, D. McMorrow** (**2001**), *Elements of Modern X-Ray Physics*. (Ed.), Wiley.

[13]   **J. D. Jackson** (**1998**), *Classical Electrodynamics*. (Ed.), Wiley.

[14]   **A. Duri** (**2006**). *Dynamique spatialment et temporellement hétérogène dans la relaxation lente del la matière molle vitreuse*. Ph.D. thesis, Universitè Montpellier.

[15]   **G. Adam, J. H. Gibbs (1965)**. *On the Temperature Dependence of Cooperative Relaxation Properties in Glass-Forming Liquids*. In *Journal of Chemical Physics*, **43**, p. 139-146.

[16]   **A. Einstein (1905)**. *Über die von der molekularkinetischen Theorie der Wärme geforderte Bewegung von in ruhenden Flüssigkeiten suspendierten Teilchen*. In *Annalen der Physik*, **17**, p. 549-560.

[17]   **P.N. Pusey** (**1991**), *Liquids, Freezing and the Glass Transition*. (Ed.), Elsevier, Amsterdam.

[18]   **P. G. Debenedetti, F. H. Stillinger (2001)**. *Supercooled liquids and the glass transition*. In *Nature*, **410**, p. 259-267.

[19]   **L. Cipelletti, L. Ramos, S. Manley, E. Pitard, D. A. Weitz,b**

E. E. Pashkovskid, M. Johansson (2003). *Universal non-diffusive slow dynamics in aging soft matter*. In *Faraday Discussions*, **123**, p. 237-251.

[20]   **D. R. Reichman, P. Charbonneau (2005)**. *Mode-coupling theory.* In *Journal of Statistical Mechanics: Theory and Experiment*, **-**, p. P05013.

[21]   **F. H. Stillinger (1995)**. *A Topographic View of Supercooled Liquids and Glass Formation*. In *Science*, **267**, p. 1935-1939.

[22]   **G. Brambilla, D. El Masri, M. Pierno, L. Berthier, L. Cipelletti, A. Schofield, (2009)**. *Probing the Equilibrium Dynamics of Colloidal Hard Spheres above the Mode-Coupling Glass Transition*. In *Physical Review Letters*, **102**, p. 085703.

[23]   **R. Richert (2002)**. *Heterogeneous dynamics in liquids: fluctuations in space and time*. In *Journal of Physics: Condensed Matter*, **14**, p. R703-R738.

[24]   **L. Berthier, G. Biroli, J.-P. Bouchaud, L. Cipelletti,**

D. El Masri, D. L'Hote, F. Ladieu, M. Pierno (2005). *Direct Experimental Evidence of a Growing Length Scale Accompanying the Glass Transition*. In *Science*, **310**, p. 1797-1800.

[25]   **B. Ruta, Y. Chuskin, G. Monaco, L. Cipelletti, E. Pineda, P. Bruna, V. M. Giordano, M. Gonzalez-Silveira (2012)**. *Atomic-scale relaxation dynamics and aging in a metallic glass probed by X-ray photon correlation spectroscopy*. In *Physical Review Letters*, **109**, p. 165701.

[26]   **A. Duri, T. Autenrieth, L.-M. Stadler, O. Leupold, Y. Chushkin, G. Grubel, C. Gutt (2009)**. *Two-Dimensional Heterogeneous Dynamics at the Surface of a Colloidal Suspension*. In *Physical Review Letters*, **102**, p. 145701.

[27]   **O. Czakkel, A. Madsen (2011)**. *Evolution of dynamics and structure during formation of a cross-linked polymer gel*. In *Europhysics Letters*, **95**, p. 28001.

[28]   **H. Guo, J. N. Wilking, D. Liang, T. G. Mason, J. L. Harden, R. L. Leheny (2007)**. *Slow, nondiffusive dynamics in concentrated nanoemulsions*. In *Physical Review E: Statistical, Nonlinear, and Soft Matter Physics*, **75**, p. 041401.

[29]   **A. Fluerasu, A. Moussaid, A. Madsen, A. Schoeld (2007)**. *Slow dynamics and aging in colloidal gels studied by x-ray photon correlation spectroscopy*. In *Physical Review E: Statistical, Nonlinear, and Soft Matter Physics*, **76**, p. 010401.

[30]   **J.P. Bouchaud, E. Pitard (2001)**. *Anomalous dynamical light scattering in soft glassy gels*. In *European Physical Journal E: Soft Matter*, **6**, p. 231-236.

[31]   **P. Kwasniewski** (**2012**). *Probing dynamics of hard sphere suspensions at high volume fractions with coherent X-rays*. Ph.D. thesis, Joseph Fourier University, Grenoble.

[32]   **A. Duri, L. Cipelletti (2006)**. *Length scale dependence of dynamical heterogeneity in a*

colloidal fractal gel. In *Europhysics Letters*, **76**, p. 972.

[33]   **A. Madsen, R. L. Leheny, H. Guo, M. Sprung, O. Czakkel (2010)**. *Beyond simple exponential correlation functions and equilibrium dynamics in x-ray photon correlation spectroscopy*. In *New Journal of Physics*, **12**, p. 055001.

[34]   **H. Winick, G. Brown, K. Halbach, J. Harris (1981)**. *Wiggler and Undulator Magnets*. In *Physics Today*, **34**, p. 50-63.

[35]   **X. Llopart, M. Campbell, R. Dinapoli, D. San Segundo, E. Pernigotti (2002)**. *Medipix2: a 64-k Pixel Readout Chip With 55-micron Square Elements Working in Single Photon Counting Mode*. In *IEEE Transactions on Nuclear Science*, **49**, p. 2279-2283.

[36]   **L. Cipelletti, L. Ramos (2005)**. *Slow dynamics in glassy soft matter*. In *Journal of Physics: Condensed Matter*, **17**, p. R253-R285.

[37]   **L. Cipelletti, S. Manley, R. C. Ball, D. A. Weitz (2000)**. *Universal Aging Features in the Restructuring of Fractal Colloidal Gels*. In *Physical Review Letters*, **84**, p. 2275-2278.

[38]   **D. Orsi, L. Cristofolini, M. P. Fontana, E. Pontecorvo, C. Caronna, A. Fluerasu,**

F. Zontone, A. Madsen (2010). *Slow dynamics in an azopolymer molecular layer studied by x-ray photon correlation spectroscopy.* In *Physical Review E: Statistical, Nonlinear, and Soft Matter Physics*, **82**, p. 031804.

[39]   **Y. Chushkin, C. Caronna, A. Madsen (2012)**. *A novel event correlation scheme for X-ray photon correlation spectroscopy.* In *Journal of Applied Crystallography*, **45**, p. 807.

9 Acknowledgements

First of all, I would like to thank all my supervisors for their guide and help during the draft of this work, and all the passion and enthusiasm they have transmitted to me.

In particular:

- Dott. *Beatrice Ruta* (sorry professor, ladies first), to whom I owe my survival in Grenoble, and for all the <u>very</u> scrupulous observation of my work here on ESRF.
- Prof. *Luigi Cristofolini*, first of all for believing in my capacity and giving me the opportunity to join this project, (I hope to have not deluded him) and of course the guidance and support through all the stages of this work.
- Dott. *Davide Orsi*, who was invaluable in transmitting me all his precedent work ad experience in the subject. I begun this work stepping on his shoulders.

I'd like to thank also all the ID10 staff for their friendship and hospitality.

I haven't forgot my family, who have supported me during all this loooong years of studies, and all my friends (old and new) who are, lucky me, too much to be all written remembered here.